Stirring by Staring: Measurement-Induced Chirality

Matthew Wampler¹, Brian J. J. Khor, Gil Refael, and Israel Klich¹, ¹Department of Physics, University of Virginia, Charlottesville, Virginia 22903, USA ²Department of Physics, California Institute of Technology, Pasadena, California 91125, USA ³Institute for Quantum Information and Matter, California Institute of Technology, Pasadena, California 91125, USA

(Received 20 August 2021; accepted 7 July 2022; published 24 August 2022)

In quantum mechanics, the observer necessarily plays an active role in the dynamics of the system, making it difficult to probe a system without disturbing it. Here, we leverage this apparent difficulty as a tool for driving an initially trivial system into a chiral phase. In particular, we show that by utilizing a pattern of repeated occupation measurements we can produce chiral edge transport of fermions hopping on a Lieb lattice. The procedure is similar in spirit to the use of periodic driving to induce chiral edge transport in Floquet topological insulators, while also exhibiting novel phenomena due to the nonunitary nature of the quantum measurements. We study in detail the dependence of the procedure on measurement frequency, showing that in the Zeno limit the system can be described by a classical stochastic dynamics, yielding protected transport. As the frequency of measurements is reduced, the charge flow is reduced and vanishes when no measurements are done.

DOI: 10.1103/PhysRevX.12.031031 Subject Areas: Quantum Physics, Topological Insulators

I. INTRODUCTION

One of the most exciting goals of the field of quantum dynamics is to be able to control the microscopic motion of particles in a reliable and universal way. Floquet engineering, coupled with our knowledge of topological quantum phases, presented one such route and brought about new paradigms for the quantum control of atomic and electronic motion. A periodic modulation of the Hamiltonian was shown to induce Chern bands in nontopological semiconductors as well as graphene, and this remarkable feat was observed in a variety of solid-state and atomic systems [1-3].

The range of drive-induced topological phases kept growing over the past decade to include states with no static analogs. A prominent example is the anomalous Floquet Anderson insulator [4–7]. In this 2D phase, a chiral edge state emerges alongside completely trivial bulk bands in stark contrast to standard topological edge states which are spectrally connected to bulk bands. Thus, such an insulator avoids issues associated with fermion anomalies. The trick behind this phase is a Floquet Hamiltonian modulation which alters the hopping along a square lattice

Published by the American Physical Society under the terms of the Creative Commons Attribution 4.0 International license. Further distribution of this work must maintain attribution to the author(s) and the published article's title, journal citation, and DOI.

in a sequence that stirs the particles [8] in such a way that bulk motion is canceled and edge states emerge.

An additional tool for control, however, is measurement (see, e.g., Refs. [9,10]). "Dark-state" engineering was explored as a means to stabilize a variety of phases through measurement or decay processes that eliminate unwanted elements in the wave function in order to stabilize a desired steady state [11–15]. The challenge in this approach is to engineer the necessary projectors. The combination of periodic driving and dissipation has also been discussed [16,17]. More recently, it was discovered that a combination of unitary evolution and measurement could actually induce a transition between highly entangled quantum states into low entanglement classical-looking states at high measurement frequency [18-25]. The study of the competing effects of projective measurement and unitary evolution has also been intensely researched in the context of quantum circuit models [26-40]. The physics of measurement-induced phase transitions has been studied in the context of measurement protected quantum orders [33], symmetry-protected topological phases [38], geometric phase [41], many-body localization [42], and various aspects of entanglement measures [26,28,37,39,40,43]. There are also recent works which study the entanglement transitions with measurement and unitary evolution for free fermions hopping on a 1D chain [19,44,45]. In Ref. [46] the competing effects of unitary evolution and measurements were studied using a closed hierarchy approach. This method was used to describe nonequilibrium steady states of current [46] as well as density fluctuations (quantum wakes) following a moving particle detector and other disturbances [47].

mbw5kk@virginia.edu

Tik3j@virginia.edu

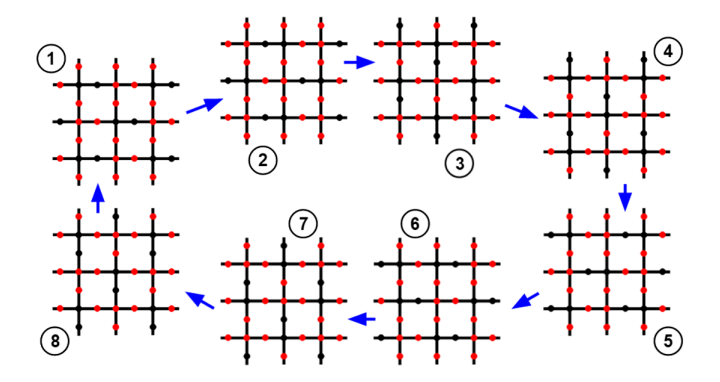


FIG. 1. Measurement protocol. Red vertices indicate the set of repeatedly measured sites, while black sites are unmeasured (the free evolving sets, A_i). The adjacent pairs of black vertices trace out an inherently chiral (in this case clockwise) path along a decorated square inside the Lieb lattice. The path can be made counterclockwise if the order of the eight steps is reversed.

In this paper we combine these developments to show that measurements can stabilize protected edge transport. All that is needed is a sequence of local occupation measurements which serve to herd particles into circular orbits. These circular orbits then play a somewhat similar role to the semiclassical orbits used to illustrate the quantum Hall effect [48,49] where particles take closed trajectories in the bulk while the presence of an edge induces chiral motion via "skipping orbits" [50]. The result, so-called stirring by staring, combines the pioneering ideas of dark-state engineering with Floquet engineering to generate exotic protected edge dynamics. As a simple

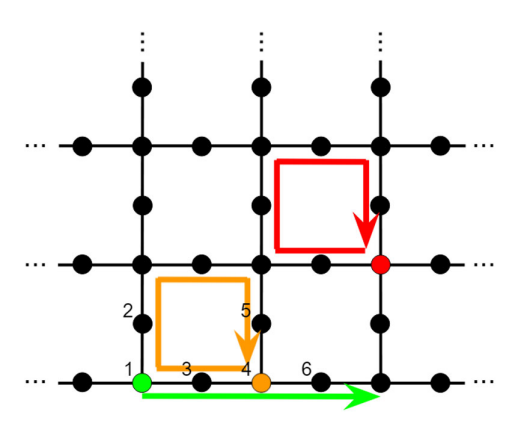


FIG. 2. Particle trajectories on the Lieb lattice under the measurement protocol in the infinite measurement (Zeno) limit with the perfect switching cycle $(T/8 = \pi/2)$. In this regime, evolution becomes deterministic and particle trajectories can be seen explicitly. Particles localized in the bulk (red) at the start of the protocol and particles initialized at sites of type 3 or 4 (orange) on the edge trace out a closed loop after no more than five measurement cycles. On the other hand, particles initialized at sites of type 1 (green) or 6 on the boundary at the beginning of the protocol propagate along the edge, shifting by 1 dynamical unit cell every two measurement cycles (see Appendix H for details).

example, we show how this can be accomplished on a Lieb lattice where chirality is achieved via an eight-step measurement pattern.

We show that our measurement scheme, illustrated in Fig. 1 and explained in detail below, yields no net transport of particles in the bulk of the lattice. However, when the system has an edge, it will induce movement of particles along the edge; see Fig. 2. We explore the evolution of particle density in the system using the closed hierarchy method [46] both by direct numerical simulation as well as by analytically studying the Zeno limit of rapid measurements. The transport in the Zeno limit, and in a perturbative regime of large but finite measurement frequency near the Zeno limit, can be conveniently described as a stochastic process. In this regime, we prove that the boundary transport is protected from a wide range of edge perturbations including random potentials, hopping energies, edge deformations, and site removal. It is critical to note that such protection cannot be achieved in a 1D system (with a strictly local Hamiltonian), where a removal of a small set of sites can simply disconnect the system into disjoint parts with no possibility of transport.

II. PROTOCOL

The measurement cycle consists of eight steps taking an overall time T. At each step, we take repeated snapshots of the presence of particles throughout a subset of the lattice, while the system is allowed to evolve freely between the measurements. We denote the set of sites *not* being measured at step i by A_i as marked in Fig. 1, and enforce periodicity by setting $A_{i+8} = A_i$. Within each step, the following procedure is followed.

- (1) Particle densities at all sites in $(A_i \cap A_{i-1})^c$ are measured.
- (2) Free evolution under a free hopping Hamiltonian $\mathcal{H} = -t_{\text{hop}} \sum_{\langle \mathbf{r} \mathbf{r}' \rangle} a^{\dagger}_{\mathbf{r}} a_{\mathbf{r}'}$ for a time $\tau = (T/8n)$. Here, n is an integer describing the measurement frequency.
- (3) Particle densities at all sites in A_i^c are measured.
- (4) Steps 2 and 3 are repeated *n* times.

For convenience, throughout the paper we set $t_{\rm hop}=1$ and $\hbar=1$. For clarity, we note here that in the rest of the paper we refer to one complete iteration of the full eight-step procedure as a "full measurement cycle" or sometimes just "measurement cycle." On the other hand, each of the individual steps within the eight-step procedure are referred to as a "measurement step."

The steps detailed above correspond to a sequence of maps on the density matrix ρ of the system. Two distinct elements are involved in the dynamics. First, the measurement of the presence of a particle at a lattice site \mathbf{r}_i can be represented by the Krauss map $\rho \to n_i \rho n_i + (1 - n_i)\rho(1 - n_i)$, with $n_i = a_i^{\dagger}a_i$ the number operator for the site. In between such measurement steps we have

unitary evolution, which is described, as usual, via $\rho \to U \rho U^{\dagger}$, where U is a many-body evolution operator.

To describe the densities and correlations in the system, we concentrate on the iterative evaluation of two-point correlation operators:

$$G_{\mathbf{r}\mathbf{r}'}(t) = \text{Tr}[\rho(t)a_{\mathbf{r}}^{\dagger}a_{\mathbf{r}'}]. \tag{1}$$

The two-point correlation has a closed evolution equation under particle density measurements and free evolution operations, as long as the free evolution is noninteracting [46]. The change in G due to the Krauss map associated with single site particle density measurement can be shown to imply eliminating correlations between the measured site and other sites [46]. Explicitly, one can check that the measurement of particle presence at a lattice site \mathbf{r} is described by the map,

$$G \to (1 - P_{r})G(1 - P_{r}) + P_{r}GP_{r},$$
 (2)

where $P_{\bf r}=|{\bf r}\rangle\langle{\bf r}|$ is the (single-particle) projector onto site ${\bf r}$. For noninteracting evolution, fermion operators transform as ${\cal U}^\dagger a_{\bf q}^\dagger {\cal U} = U_{{\bf q}{\bf q}'} a_{{\bf q}'}^\dagger$, where ${\cal U}$ is called a single-particle evolution. In this case ${\cal G}$ transforms as

$$G \to UGU^{\dagger}$$
. (3)

In the case of interest for us here, we take $U = e^{-i\tau H}$, where $H = \sum_{\langle \mathbf{r}, \mathbf{r}' \rangle} |\mathbf{r}\rangle \langle \mathbf{r}'|$, describing free hopping of the fermions on the lattice.

To study the repeated application of these maps to G, it is convenient to view G as a vector in $\mathcal{H}_{\text{double}} = \mathbb{C}^{\mathcal{N}^2}$, where \mathcal{N} is the total number of fermion sites. We write $G = \sum_{\mathbf{r}\mathbf{r}'} G_{\mathbf{r}\mathbf{r}'} |\mathbf{r}\rangle \langle \mathbf{r}'| \to G = \sum_{\mathbf{r}\mathbf{r}'} G_{\mathbf{r}\mathbf{r}'} |\mathbf{r}\rangle \otimes |\mathbf{r}'\rangle$, and the evolution of G under the maps above can be notated as

$$G(t+T) = \Lambda G(t), \tag{4}$$

where Λ is the (super)operator acting on G corresponding to the eight-step measurement protocol given in the previous section. To construct Λ , we write the transformation associated with free evolution and with particle measurement, respectively, as

$$G \to (U \otimes \bar{U})G,$$
 (5)

$$G \to \pi_{\mathbf{r}} G,$$
 (6)

where $\pi_{\mathbf{r}} \equiv (1 - P_{\mathbf{r}}) \otimes (1 - P_{\mathbf{r}}) + P_{\mathbf{r}} \otimes P_{\mathbf{r}}$. If all the sites in a set A^c are measured simultaneously, we find (see Appendix D) that the combined operation on G becomes

$$\prod_{\mathbf{r}\in A^c} \pi_{\mathbf{r}} \equiv \Pi_A = \sum_{\mathbf{r}\in A^c} P_{\mathbf{r}} \otimes P_{\mathbf{r}} + P_A \otimes P_A, \tag{7}$$

where

$$P_A \equiv \sum_{\mathbf{r} \in A} P_{\mathbf{r}}.\tag{8}$$

Note that $(\Pi_A G)_{\mathbf{rr'}} = G_{\mathbf{rr'}}$ if both sites $\mathbf{rr'}$ are in the unmeasured set A; on the other hand, if \mathbf{r} or $\mathbf{r'}$ are in A^c , we have $(\Pi_A G)_{\mathbf{rr'}} \delta_{\mathbf{rr'}}$. In other words, the correlations between the measured sites A^c and all other sites are destroyed while acting as an identity on the subspace A of unmeasured sites. It is important to note that Π_A is itself a projection operator on $\mathcal{H}_{\text{double}}$. To see this, note that the operators $\pi_{\mathbf{r}}$ form a set of commuting orthogonal projectors, and consequently their product is an orthogonal projector. Another useful property that follows is that

$$\Pi_B \Pi_A = \Pi_{A \cap B}. \tag{9}$$

We are now in position to write the evolution operator Λ describing a cycle of measurements and evolution as described by the measurement protocol above. Explicitly, after each cycle, which involves eight steps each repeated n times, $G \to \Lambda G$ with

$$\Lambda = [\Pi_{A_8}(U \otimes \bar{U})\Pi_{A_8}]^n [\Pi_{A_7}(U \otimes \bar{U})\Pi_{A_7}]^n \cdots [\Pi_{A_1}(U \otimes \bar{U})\Pi_{A_1}]^n.$$
 (10)

We now turn to analyze the dynamics described by this operator.

III. ZENO LIMIT

We first study the operator Λ , of Eq. (10), in the limit of many measurements per cycle (i.e., $n \to \infty$). The dynamics under high frequency repeated measurements is known as the quantum Zeno limit. The signature characteristic of this regime is the freezing of evolution in the subspace of measured sites. The Zeno effect (and the closely related anti-Zeno effect) has a long history [51] with broad applications including, for example, counterfactual quantum computing and communication [52,53] and loss suppression in ultracold molecule experiments with strong, long-range dipolar interactions [54,55]. Over the past 30 years, the Zeno and related effects have been observed experimentally across a variety of physical systems [56–62].

Let us first consider one of the eight steps in Eq. (10). Formally expanding in $\tau = (T/8n)$, we find that

$$[\Pi_A(U \otimes \bar{U})\Pi_A]^n = \Pi_A(U_A^n \otimes \bar{U}_A^n)\Pi_A + O(\tau^2 n). \tag{11}$$

Here, $U=e^{-i\tau H}$ and $U_A=e^{-i\tau H_A}$, where $H_A\equiv P_AHP_A$. To get Eq. (11), we first expand each measurement or evolution step in τ :

$$\begin{split} \Pi_A(U \otimes \bar{U})\Pi_A &= \Pi_A(I - i\tau[H \otimes I - I \otimes H])\Pi_A + O(\tau^2) \\ &= \Pi_A e^{-i\tau\Pi_A[H \otimes I - I \otimes H]\Pi_A}\Pi_A + O(\tau^2). \end{split} \tag{12}$$

A short calculation (see Appendix D) shows that

$$\Pi_A[H \otimes I - I \otimes H]\Pi_A = H_A \otimes P_A - P_A \otimes H_A; \tag{13}$$

hence,

$$\Pi_A(U \otimes \bar{U})\Pi_A = \Pi_A(U_A \otimes \bar{U}_A)\Pi_A + O(\tau^2), \quad (14)$$

which, using $[U_A \otimes \bar{U}_A, \Pi_A] = 0$, gives Eq. (11). The expression (11) shows that, in the Zeno limit, the average evolution is dominated by local evolution in the region A and suppresses hopping into the measured sites A^c . Finally, plugging Eq. (11) into Eq. (10), we find

$$\Lambda = \Pi_{A_8} (U_{A_8}^n \otimes \bar{U}_{A_8}^n) \Pi_{A_8 \cap A_7} (U_{A_7}^n \otimes \bar{U}_{A_7}^n)
\cdots \Pi_{A_7 \cap A_1} (U_{A_1}^n \otimes \bar{U}_{A_1}^n) \Pi_{A_1} + O(\tau^2 n).$$
(15)

Next, we use this result to formally describe evolution for N cycles, when $Nn\tau^2 \ll 1$, and $n\tau$ is kept constant.

IV. STOCHASTIC DESCRIPTION OF THE ZENO LIMIT

The local nature of the evolution in the Zeno limit (15) leads to a striking simplification that we now describe. We observe that, if one only follows the local particle density given by the diagonal elements G_{rr} , the evolution is given by a periodic classical stochastic process. To see this, note that the evolution of G in the Zeno limit consists of steps of the form

$$G \to U_{A_i}^n G U_{A_i}^{n\dagger}.$$
 (16)

Each set A_i consists of the union of pairs of neighboring sites, the black sites in Fig. 1. Since the pairs forming A_i are disjoint, the evolution U_{A_i} can only develop nontrivial correlations between the sites of the same pair. Consider a pair of such sites. After the evolution, all sites are measured except for sites in $A_i \cap A_{i+1}$, which is a set of isolated points on the lattice; in particular, any correlations (nondiagonal terms in G) developed between the pair of sites in A_i would be set to zero once the site in A_i but not in A_{i+1} is measured (long-range correlations between sites in $A_i \cap$ A_{i+1} are not annihilated, but will be annihilated in the next step, and cannot be generated by any of the U_{A_i}). Thus, if we start with a diagonal G, it will remain diagonal throughout the evolution. Moreover, even if we start with some nonzero off-diagonal terms, these will be quickly annihilated by the measurements. Thus we should be able to describe the evolution, in the Zeno limit, just in terms of the dynamics of the diagonal of G. Indeed, note that G_{rr} are real non-negative numbers and the total number of particles $\sum_{\mathbf{r}} G_{\mathbf{rr}}$ is a constant of motion, and thus $G_{\mathbf{rr}}$ can be treated (up to normalization) as probabilities, and the process describing the evolution is a classic stochastic process.

Explicitly, if we represent the density at time t as a vector $|g(t)\rangle$ defined via

$$[g(t)]_{\mathbf{r}} \equiv G_{\mathbf{rr}}(t),\tag{17}$$

then in the Zeno limit the density evolves via Markovian dynamics as

$$|g\rangle \to R_{\rm cvc}|g\rangle,$$
 (18)

where the transition matrix R_{cyc} consists of the eight steps of our process; namely,

$$R_{\text{cvc}} = R_8 R_7 R_6 R_5 R_4 R_3 R_2 R_1. \tag{19}$$

The transition matrices R_i are defined as follows. Each unmeasured set A_i is associated with two site types α , β that are not being measured, as described in Fig. 3 (e.g., A_1 is the union of all sites of types 1,3; A_2 is the union of sites 3,4; etc.). The unitary evolution associated with a given unmeasured set A_i , breaks into a sum of pairs of nearest neighbors:

$$U_{A_i} = I_{A_i^c} \bigoplus_{\langle \alpha, \beta \rangle \in A_i} e^{i\tau n \sigma_x}. \tag{20}$$

Next, we apply the evolution (16) and then measure all sites except those in $A_i \cap A_{i+1}$, which has the effect of eliminating off-diagonal elements in G. Consider one of the pairs of sites $\langle \alpha, \beta \rangle \in A_i$ and an initially diagonal $G = \mathrm{diag}(g_1, g_2)$. Applying the evolution (20) to get $e^{i\tau n\sigma_x}Ge^{-i\tau n\sigma_x}$ and

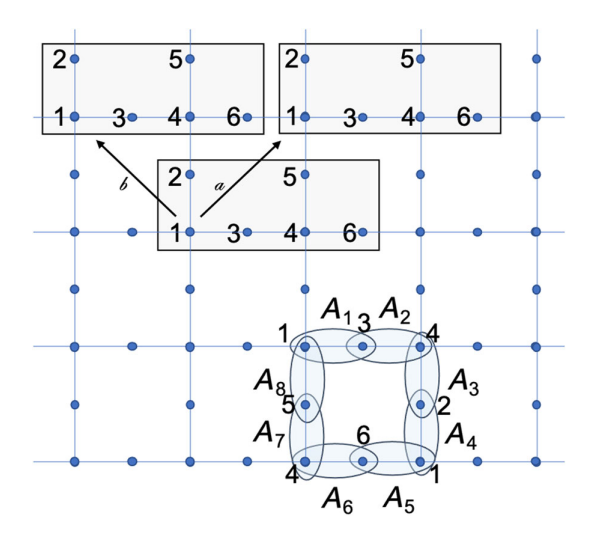


FIG. 3. The unit cell for the measurement driven Lieb lattice dynamics consists of two Lieb lattice unit cells. A choice for such a dynamical unit cell is depicted.

then setting the of-diagonal elements to zero, we get a new diagonal matrix G with $G = \text{diag}[\cos^2(n\tau)g_1 +$ $\sin^2(n\tau)g_2,\cos^2(n\tau)g_2+\sin^2(n\tau)g_1$]. In other words, a particle located in one of the sites jumps to the other site with probability

$$p = \sin^2(n\tau) = \sin^2\left(\frac{T}{8}\right),\tag{21}$$

or stays with probability 1 - p. A particle in any other position will not move. Therefore,

$$R_i = \bigoplus_{\langle \alpha, \beta \rangle \in A_i} \begin{pmatrix} 1 - p & p \\ p & 1 - p \end{pmatrix} \bigoplus_{\text{other sites}} I. \quad (22)$$

This defines a periodically driven random walk. We note that the transition matrices R_i are bistochastic matrices, and thus so is $R_{\rm cvc}$.

A remark is in order here about Eq. (22). In a system with a boundary, a set A_i may include isolated sites that do not have an adjacent neighbor also in A_i . For example, consider the boundary of the lattice in Fig. 3. The set A_3 as defined includes sites of type 4 and 2; however, looking at the lower boundary, we see that sites of type 4 on the boundary do not have an adjacent site of type 2. Similarly to the measured sites, the dynamics for these isolated elements of A_i are frozen in the Zeno limit. In Eq. (22), the isolated elements of A_i are included in "other sites" since they are not part of an adjacent pair in A_i .

The particular choice $T=4\pi$ leads to p=1. We refer to this choice as "perfect switching." In this case, R_{cyc} is a permutation matrix, and the motion of particles is deterministic. Of course, on the other hand, when $T = 8\pi$, p = 0 and there is no evolution at all.

We now consider the counting statistics of transport to the right per cycle. To do so, we attach a counting field $e^{i\theta}$ to each horizontal link, by modifying the above transition matrices of R_1 , R_2 , R_5 , R_6 to

$$R_{i} = \bigoplus_{\langle \alpha, \beta \rangle \in A_{i}} \begin{pmatrix} 1 - p & e^{i\theta} p \\ e^{-i\theta} p & 1 - p \end{pmatrix} \bigoplus_{\text{other sites}} I, \quad (23)$$

whenever α , β are nearest neighbors on a horizontal line, such that α is to the left of β .

With the counting field present, we can introduce the moment generating function,

$$\chi_{N}(\theta) \equiv \sum_{ij} \sum_{w: i \to j} e^{i\theta l(w)} \operatorname{Prob}_{N}(w) G_{ii}(0)$$

$$= \sum_{ij} [R_{\text{cyc}}(\theta)^{N}]_{ij} G_{ii}(0) = \langle I | R_{\text{cyc}}^{N}(\theta) | g_{0} \rangle, \quad (24)$$

where $w: i \to j$ is a sequence of hops from site i to site j, $Prob_N(w)$ is the probability for the path w after N

measurement cycles using the transition matrix R_{cyc} , and l(w) is the net number of hops in the x direction. In the next line, $|g_0\rangle$ is the initial density distribution at t=0 and $|I\rangle$ is a vector whose elements are all 1 (corresponding to G = I).

We can use χ_N to compute quantities of interest, most important of which is the flow, defined as the total displacement per cycle, per unit length. The flow in the x direction is given by

$$F = \lim_{N \to \infty} F_N, \tag{25}$$

where F_N is the average flow in the first N cycles,

$$F_N = \frac{1}{L_x} \frac{1}{N} i \partial_{\theta} \chi_N(\theta)|_{\theta=0}, \tag{26}$$

with L_x the length in the x direction.

A. Absence of bulk transport

In a translation invariant situation, it is convenient to work in momentum space. Here, we must use the "dynamical unit cell" where the periodic evolution happens, which is double the Lieb lattice's original unit cell (see Fig. 3).

The Bravais lattice for the dynamical unit cell is a rotated square lattice whose primitive Bravais vectors are marked as a, b in Fig. 3. Below, we use n, m to denote the position of the unit cell and $\mu, \nu \in \{1, ..., 6\}$ to denote the individual atom inside the cell. We can then write

$$R_i(\mathbf{n}, \mu; \mathbf{m}, \nu) = \int \frac{d^2k}{2\pi} R_i(\mathbf{k}, \mu, \nu) e^{i\mathbf{k}\cdot(\mathbf{n}-\mathbf{m})}.$$
 (27)

For example, R_5 , is associated with A_5 , which includes sites 1,6 in neighboring dynamic unit cells; hence,

The work consider the counting statistics of transport to ght per cycle. To do so, we attach a counting field
$$e^{i\theta}$$
 ch horizontal link, by modifying the above transition ces of R_1 , R_2 , R_5 , R_6 to
$$R_i = \bigoplus_{\langle \alpha,\beta \rangle \in A_i} \begin{pmatrix} 1-p & e^{i\theta}p \\ e^{-i\theta}p & 1-p \end{pmatrix} \bigoplus_{\text{other sites}} I, \quad (23)$$

$$R_5(k,\theta) = \begin{pmatrix} 1-p & 0 & 0 & 0 & 0 & pe^{-i(\theta+k\cdot(a-b))} \\ 0 & 1 & 0 & 0 & 0 & 0 \\ 0 & 0 & 1 & 0 & 0 & 0 \\ 0 & 0 & 0 & 1 & 0 & 0 \\ 0 & 0 & 0 & 0 & 1 & 0 \\ pe^{i(\theta+k\cdot(a-b))} & 0 & 0 & 0 & 0 & 1-p \end{pmatrix}.$$

In the deterministic case, p = 1, we find for the full cycle:

$$\chi_{N}(\theta) \equiv \sum_{ij} \sum_{w: i \to j} e^{i\theta l(w)} \operatorname{Prob}_{N}(w) G_{ii}(0) \\ = \sum_{ij} [R_{\operatorname{cyc}}(\theta)^{N}]_{ij} G_{ii}(0) = \langle I | R_{\operatorname{cyc}}^{N}(\theta) | g_{0} \rangle, \quad (24)$$

$$R_{\operatorname{cyc}}(k, \theta) = \begin{pmatrix} 1 & 0 & 0 & 0 & 0 & 0 \\ 0 & 0 & e^{i\theta} & 0 & 0 & 0 \\ 0 & 0 & 0 & e^{i\theta} & 0 & 0 \\ 0 & 0 & 0 & 0 & 1 & 0 \\ 0 & 0 & 0 & 0 & 0 & e^{ik \cdot b} e^{-i\theta} \\ 0 & 0 & e^{-ik \cdot b} e^{-i\theta} & 0 & 0 & 0 \end{pmatrix}.$$
where $w: i \to j$ is a sequence of hops from site i to site j , rob_N(w) is the probability for the path w after N (28)

It is possible to check that in this case, with p=1, $R_{\rm cyc}(k,\theta)^5=I$. Therefore, the system returns to itself after 5 cycles without generating any transport at all. For $p \neq 1$, we find that ${\rm ReTr}R_{\rm cyc}(k,\theta)^n$ is a symmetric function of θ , and here too, there is no transport after an arbitrary number of cycles. To do so, we computed the characteristic polynomial of the matrix $R_{\rm cyc}(k,\theta)$ and found that it is equal to that of $R_{\rm cyc}(-k,-\theta)$, implying equality of eigenvalues of the matrices.

It is also possible to check that for any $k_x, k_y \neq 0$ (mod 2π), $||R_{\rm cyc}|| < 1$, which implies the longtime behavior will be dominated only by the k=0 component of the initial distribution. For $k_x = k_y = 0$ and $\theta = 0$ there is a single left and right eigenvector with eigenvalue 1, which is the uniform density state $|I\rangle$, implying that up to exponentially small corrections, the current density (26) vanishes.

B. Edge transport

We have concluded that there is no bulk transport associated with the stochastic process defined by R_{cvc} , for any p. In this section, we contrast the situation to when an edge is present. We implement the dynamics by removing all sites beyond the physical edges (e.g., sites with y < 1) and removing any transitions involving sites beyond the edges from the dynamics. We start with the deterministic case, namely, p = 1. In Fig. 2, we exhibit a half plane with an edge. For p = 1, we can track the motion of each particle and conclude that bulk particles perform a closed loop. On the other hand, particles starting at the edge divide into two sets: some of the edge particles (6,1) perform a motion along the edge, while some (3,4) perform a closed loop. Thus, if we start from an initial state where particles are placed along the edge, we will have particle transport along the edge (particles 6,1 will move to the right). This behavior is clearly analogous to the familiar skipping orbits in the semiclassical description of the integer quantum Hall effect.

What will happen away from p = 1? Consider first the case of a strip with periodic boundary conditions in the long direction (say, x) and open boundary conditions in the ydirection with L_{ν} dynamical unit cells in the y direction. Let us consider states that are translationally invariant in the x direction, allowing us to analyze the behavior in Eq. (26) in momentum space. For any momentum k_x , the transition operator R can then be written as a $6L_v \times 6L_v$ matrix and analyzed. For 0 , any initially positioned particlehas a finite probability to get to any other site within a finite time and the only steady state distribution of R with eigenvalue 1 is that of uniform density (in contrast to the p = 1 case where additional steady states are possible). This distribution will be approached exponentially fast, governed by λ_2^N , where λ_2 is the second largest eigenvalue of R. In the uniform density distribution, there is no net charge transfer. Indeed in that case, the charge transfer of

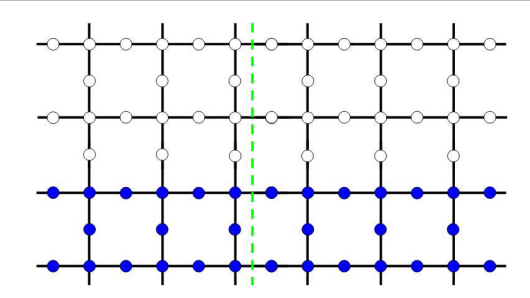


FIG. 4. Lieb lattice with lower half plane filled with particles (in blue). Trace is taken of the half plane to the right of the green dashed line. The flow across the barrier is then given by the difference between the right half trace before and after evolution.

the upper and lower edge is carried in opposite directions and cancels.

To get net transfer, we initially place particles only close to one of the edges. In a finite width system, away from the perfect switching cycle, we expect the charge transport to be transient: once the measuring protocol starts, it will transport a finite amount of particles while also spreading particles toward the second edge, rapidly approaching the uniform density state. Thus, to study the net particle flow associated with a given edge we must work in the thermodynamic limit $(L_y \to \infty)$, or, more precisely, $L_y \gg T_w$, where T_w is the typical time it may take a particle to diffuse from the middle of the sample to one of the edges.

We now numerically compute the number of particles F that flow across a slice through the Lieb lattice during evolution (see Fig. 4). In other words, we compare the number of particles to the left of the slice before and after the application of Λ , computing

$$F_{\text{sim}} \equiv \sum_{\mathbf{r} \text{ to the left of slice}} [(\Lambda G)_{\mathbf{rr}} - G_{\mathbf{rr}}]. \tag{29}$$

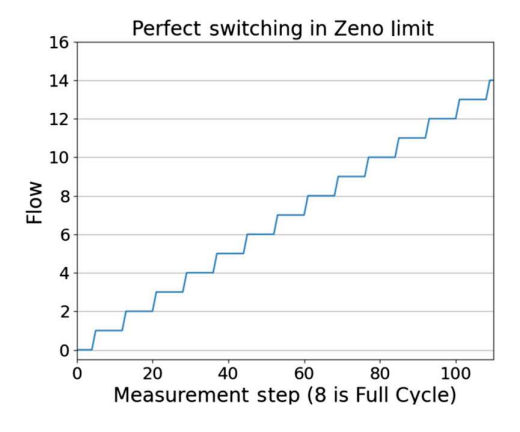


FIG. 5. Charge transfer of the left half filled plane in the Zeno limit with $(T/8) = (\pi/2)$; namely, p = 1. In this section, the Lieb lattice size for all simulations is 33×33 unless otherwise stated. Here, precisely one particle is transported across the flow cut during the eight-step measurement cycle.

This is done by initiating the system at $G(t=0)=G_0$, where G_0 is a diagonal matrix corresponding to particles placed on the bottom half of a square lattice, with open boundary conditions. We then iterate the map (10), computing $\Lambda^N G_0$, increasing N but being careful to limit the number of cycles to remain within the regime that no significant density has had time to build up close to the upper edge.

The combination of the Zeno limit with the perfect switching point p=1 leads to a clearly quantized flow, as is clearly exhibited in Fig. 5, and can be understood by tracking the trajectories of the particles (see Fig. 2 and Appendix H for details of the motion). Next we will consider both the cases of $p \neq 1$ as well as the non-Zeno limit.

V. CHARGE TRANSPORT: BULK-EDGE DECOMPOSITION

We now turn to calculating the charge transport per measurement cycle in the Zeno limit with arbitrary p. The result is described in Fig. 6. Since the bulk transport vanishes for any p, the flow will still be completely localized near the edge. Below, we exhibit an analytical formula for the flow, Eq. (30), achieved using a bulk-boundary decomposition in the limit $L_y \to \infty$ (and verify it by direct numerical simulations of the dynamics on finite systems). The resulting dependence on p is shown in Fig. 6, exhibiting a crossover behavior ranging from the integer transport at p=1 to no transport when p=0 (where the dynamics is trivial, since all hopping is blocked).

We show how the edge flow can be written in terms of bulk operators. This correspondence between the bulk properties of the system and the charge transport on the edge both provides a direct, efficient method to calculate the flow and implies the robustness of the flow to any perturbations near the boundary of the system.

To observe the flow we imagine an infinite strip in the x direction. We partition the strip into 3 regions as shown in Fig. 7. The bottom region of the system (below height ℓ_1) is completely filled with particles, while the top (above ℓ_2) is empty. In between ℓ_1 and ℓ_2 , the particle density is left

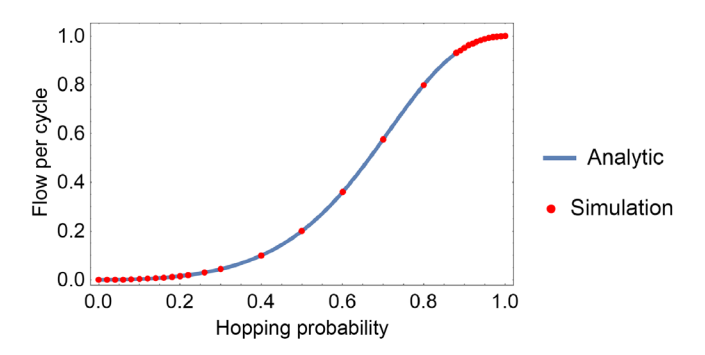


FIG. 6. Charge transport per measurement cycle in the Zeno limit. The analytic formula given in Eq. (30) is compared with the transport found from direct simulation for a selection of hopping probabilities.

arbitrary and will have no effect on the particle transport. This choice isolates the flow along just the bottom edge of the system, removing the equal and opposite contribution from the flow along the top edge. Charge distributions of this type are analogously used as a tool to calculate charge flow along an edge in the context of Floquet topological insulators; see, for instance, Ref. [63]. In Appendix E we prove that

$$F = F_{\text{bulk}} + F_{\text{edge}},\tag{30}$$

where

$$F_{\text{bulk}} = i \sum_{\alpha \beta} \left[J_B(\mathbf{k}) \frac{1}{I - R_B(\mathbf{k})} \partial_{k_y} R_B(\mathbf{k}) \right]_{\alpha \beta} \Big|_{\mathbf{k} = 0}$$
(31)

and

$$F_{\text{edge}} = \frac{1}{L_x} \langle \mathbf{I} | P_{y \le 3} J P_{y \le 2} | \mathbf{I} \rangle. \tag{32}$$

Here, R_B is a bulk transition operator, equal to $R_{\rm cyc}$ except with periodic instead of open boundary conditions to make it translational invariant. The transition operators R_B , $R_{\rm cyc}$ are used to define appropriate currents $J=-i\partial_{\theta}R_{\rm cyc}(\theta)|_{\theta=0}$ and, similarly, $J_B=-i\partial_{\theta}R_B(\theta)|_{\theta=0}$. Above, for an operator A, translational invariant in x and y with respect to the unit cell of the dynamics and with matrix elements $A_{\alpha\beta}(\mathbf{r},\mathbf{r}')$, we define $A(\mathbf{k})_{\alpha\beta}$ as in Eq. (27). In the edge contribution, $P_{y\leq 2}$ is a projection operator on sites with $y\leq 2$. The above expressions are proven starting from the expression Eq. (26) for the flow F_N after a finite number of cycles and then taking the limit of large N while maintaining $N\ll \ell_1$ and keeping $\ell_2-\ell_1$ constant.

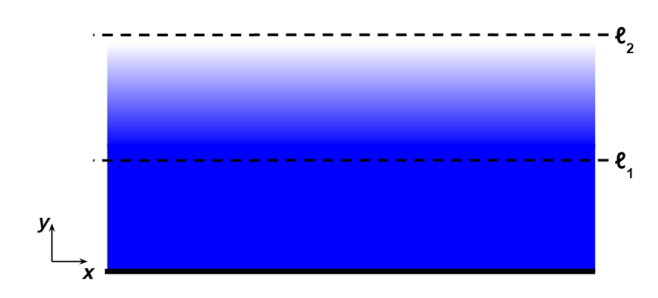


FIG. 7. Initial particle density chosen for the flow analysis. All sites below the line $y = \ell_1$ are filled with particles (shown in blue). All sites above $y = \ell_2$ are empty. The probability of finding a particle at sites in between $y = \ell_1$ and ℓ_2 is left arbitrary as the charge density in this region will not affect the flow.

To compute F_{edge} we can write, explicitly,

$$F_{\text{edge}} = \frac{1}{L_x} \sum_{\alpha\beta} \sum_{x,x'=1}^{L_x} \sum_{y'=1}^2 \sum_{y=1}^3 J_{\alpha\beta}(x,y;x',y'). \quad (33)$$

Calculating $F_{\rm edge}$ in this form we find with our measurement protocol

$$F_{\text{edge}} = p^2 + p^3 + p^4. \tag{34}$$

The contribution of $F_{\rm bulk}$ to the transport can also be evaluated readily, as it is made up of products and an inverse of 6×6 matrices and so can be easily computed for any p. In Fig. 6, we combine these two terms and compare with direct simulations of the dynamics which exhibit excellent agreement.

We now make the following especially important remark that $both \, F_{\rm bulk}$ and $F_{\rm edge}$ depend only on the bulk properties of the system (assuming weak constraints to be described below). This implies that the flow is completely insensitive to the details of the structure of the edge or local perturbations. This can be argued in the following way. We first note that

$$\langle \mathbf{I}|J|\mathbf{I}\rangle = 0; \tag{35}$$

i.e., there is zero total current in a uniform density system. Equation (35) can be seen from the form of the dynamics generated by our *R* matrices, Eq. (23), since

$$-i\partial_{\theta}|_{\theta=0}R_i|\mathbf{I}\rangle = \bigoplus_{\langle \alpha,\beta\rangle\in A_i} \begin{pmatrix} 0 & p \\ -p & 0 \end{pmatrix} \bigoplus_{\text{other sites}} I|\mathbf{I}\rangle = 0.$$

Now, consider a modification of the stochastic dynamics along the bottom edge of the system still obeying the no total current condition (35), and that there is no explicit bulk current introduced (the latter restriction of no added bulk currents may be removed upon closer analysis; see Appendix F). Assuming the current operator is short-ranged (with range of at most one unit cell), one can rewrite the expression (32) as

$$F_{\text{edge}} = \frac{1}{L_x} \langle \mathbf{I} | J P_{y \le 2} | \mathbf{I} \rangle = -\frac{1}{L_x} \langle \mathbf{I} | J P_{y > 2} | \mathbf{I} \rangle; \quad (36)$$

the expression on the right-hand side for $F_{\rm edge}$ is independent of how we vary J on the lower boundary. In other words, the global zero current condition together with the fact that the two edges responsible for the transport are physically separated means that the contribution of $F_{\rm edge}$ to the flow must be protected. Together with the bulk nature of $F_{\rm bulk}$, we see indeed a protected flow. A more detailed proof can be constructed as follows (with details in the Appendix F). Consider the following matrix, describing the perturbed dynamics:

$$R_{M}(\mathbf{r}, \mathbf{r}') = \begin{cases} \tilde{R} & r_{y}, r'_{y} \leq \ell_{1} - (N+1) \\ R_{\text{cyc}} & \ell_{1} - (N+1) \leq r_{y}, r'_{y} \leq \ell_{2} + (N+1) \\ \tilde{R}' & r_{y}, r'_{y} \geq \ell_{2} + (N+1) \\ 0 & \text{otherwise,} \end{cases}$$

$$(37)$$

where \tilde{R}, \tilde{R}' are real matrices such that R_M is doubly stochastic; i.e., R_M is identical to $R_{\rm cyc}$ in the bulk but modified near the boundary.

In Appendix F, we prove that the flow of R_M is equivalent to the flow of R_{cvc} assuming that

$$\langle \mathbf{I} | R_M(\theta = 0) = \langle \mathbf{I} | \text{ and } R_M(\theta = 0) | \mathbf{I} \rangle = | \mathbf{I} \rangle,$$
 (38)

$$\langle \mathbf{I}|J_M|\mathbf{I}\rangle = 0, \tag{39}$$

where J_M is the current operator associated with R_M . The first condition requires that R_M preserves particle number and that a uniform density is a steady state of the evolution; this implies that the transition matrix remains doubly stochastic. The second condition is the requirement that no net current can flow in the completely filled system. Note that the conditions (38) and (39) are certainly satisfied whenever R_M is a product of symmetric, doubly stochastic matrices which encapsulates a large class of physically relevant perturbations including, for example, local potentials, local variations of the hopping parameter, and removal of sites from the lattice. Indeed, repeating the argument leading to Eq. (21), including the presence of local potential terms (or variation in t_{hop}) in the local Hamiltonian will just locally change the hopping probability p, retaining the form of the dynamics as in Eq. (22)with modified p's (i.e., still made of doubly stochastic building blocks). Removal of sites can similarly be described by taking p = 0 for transitions to the removed site. Because of its stability, the flow may be viewed as a continuous topological invariant for the system. We emphasize that such protection cannot be achieved in 1D systems, which can be easily disconnected by the removal of a few sites.

A technical remark is in order here. The simulation result in Fig. 6 was computed using Eq. (29) with the cut defined as shown in Fig. 5. Therefore, the quantity computed in the simulations $F_{\rm sim}$ [Eq. (29)] is equivalent to placing the counting field θ only at a subset of the horizontal edges as opposed to placing θ on all horizontal edges as was used in defining $R_{\rm cyc}(\theta)$ through Eq. (23). Accounting for the number of edges included in the simulations—these include 2 edges per two dynamical unit cells—and that each dynamical unit cell involves 4 edges and that no charge accumulation occurs, we find simply

$$F_{\rm sim} = \frac{F}{4},\tag{40}$$

which was used in the comparison Fig. 6.

At this point, we wish to further discuss and clarify the nature of the protection of the flow in Eq. (30) and in what sense it is localized on the edge. In our setup, the charge density is constant in a thick neighborhood of the edge. It is important to emphasize, however, that the protection is not simply due to Pauli blocking, but a feature of the classical stochastic dynamics. This is evident when we consider the flow when the density in the occupied (blue) region in Fig. 7 is uniformly reduced to a lower density $\rho < 1$. In this case (especially at low density), Pauli blocking is not important for the dynamics. However, the linearity of our stochastic dynamics shows that the new flow will be $F(\rho) = \rho F(\rho = 1)$. Thus, the flow is protected (in the sense explained above) for any filling ρ , in sharp contrast with most topological insulators.

Another interesting feature of the charge transport here is that the flow we compute (for $p \neq 1$) is the result of the collective contribution of fermions that approach the edge, travel along it for a time, and then diffuse away, rather than the result of single wave packets traveling along the edge without dispersing. An alternative perspective that can help clarify the edge nature of the flow can be obtained by adding a particle sink (source) where holes (particles) can be injected (extracted) from the system. In this case holes injected in the bulk will only contribute to charge flow (for a finite time) when they reach the edge. Note that the edge flow is due to unbound charges which are only a partial contribution to the local currents in the system. For example, in the completely filled system, since the density is uniform and the R matrices are symmetric, there can be no current on any link in the system. The net zero current is the result of two different cancellations in the bulk and on the edges of the system. In the bulk, the zero current is the result of local current loops that give rise to a uniform magnetization and the net current is $\vec{\nabla} \times M = 0$. On the edge, the net current is zero as a result of cancellation between the bound currents, as in the bulk, and unbound currents that exist only on the edge. The distinction, however, between charge transport (which is localized on the edge) and current (which is not localized on the edge) is largely independent of the present work and similar distinctions must be made, for example, in discussions of Floquet topological insulators [63].

For topological insulators, a bulk gap implies that small alterations to the bulk Hamiltonian will not destroy an edge mode so long as symmetries protecting the topological phase are preserved [64]. The actual value of the current will depend on the density and on the details of how the bands are filled. Similarly, here, small changes in the carrier density will lead to changes in the magnitude of the flow, but not its existence. Interestingly, unlike topological

insulators, the existence of the flow and the protection we discuss are independent of the initial filling, which manifests itself in the off-diagonal part of G when the process starts.

On the other hand, while here the flow is robust (in the sense explained above) at any density, its value is not in general robust to arbitrary global changes of the parameters. In our system, it is possible to continuously change the flow by small extensive perturbations, say, changing the total period T. However, as stated, the exact value for the flow of the system during N cycles is protected against even strong perturbations as long as these are far enough (i.e., within a distance at least N) from the interface with the region which is not of uniform density (see Appendix F). Perturbations within the interface region may alter total charge transport values by inducing bulk currents in the system (see Fig. 15).

It is interesting to compare the behavior in the Zeno limit with a Floquet topological insulator evolution in our system which is equivalent to the one introduced in Ref. [65]. There, a periodic driving protocol is used as the source of chirality in the system, where hoppings between neighboring sites are sequentially turned on, but without any measurements. Explicitly, the analogous evolution for us, Λ_{Flog} , is

$$\Lambda_{\text{Floq}} = (U_{A_8}^n \otimes \bar{U}_{A_8}^n)(U_{A_7}^n \otimes \bar{U}_{A_7}^n) \cdots (U_{A_1}^n \otimes \bar{U}_{A_1}^n), \quad (41)$$

where we have adapted the five-step procedure on a square lattice of Ref. [65] to an analogous eight-step procedure on a

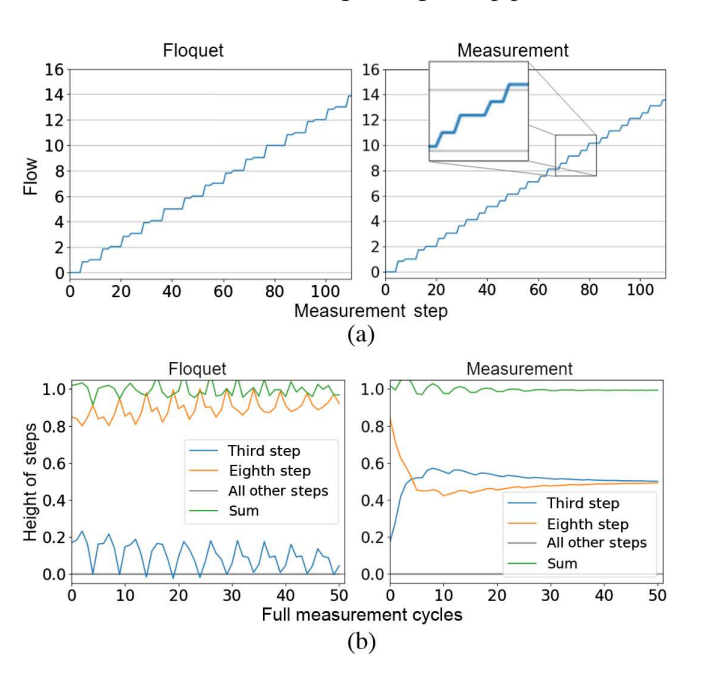


FIG. 8. (a) Charge transfer for Floquet system (left) and measurement protocol in the Zeno limit (right) where, in both cases, the hopping probability p=0.96. (b) Charge transfer after each measurement step for the Floquet system and measurement protocol with hopping probability p=0.96. Note the convergence of the third and eighth step to half the total flow per cycle.

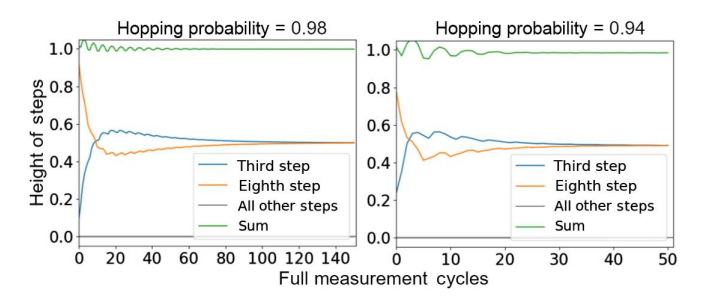


FIG. 9. Flow after each measurement step for hopping probabilities p=0.98 (left) and p=0.94 (right). Note that in the longtime limit, the third and eighth measurement step of both hopping probabilities converge to half the total flow per measurement cycle.

Lieb lattice. To simplify the comparison, we have neglected the fifth "holding period" step and sublattice potentials in the original Rudner *et al.* procedure [65].

Note the measurement protocol in the Zeno limit [Eq. (15)] is precisely the Floquet evolution interspersed with measurements between each step. Markedly, when p=1, the two evolutions are equivalent since the measurement projectors act trivially in the perfect switching case (when the initial G is diagonal).

We now turn to investigate the simulated dynamics in this regime. Away from the perfect switching cycle, p = 1, we find an interesting distinction between the Floquet evolution and the Zeno limit of the measurement or evolution cycle as shown in Fig. 8. Examining the charge transfer on the resolution of the eight steps per cycle, we find a double step structure in the charge transfer which is not present in the corresponding Floquet evolution. Namely, the third and eighth step of the measurement protocol each contribute half of the total flow per complete cycle. The reason for this double step structure is the following. The dynamics of particles in the lattice are governed by a classical, chiral random walk determined by $R_{\rm cvc}$. The third and the eighth step are the only two steps that cross the slice through the Lieb lattice, and thus all transport must occur within these two steps. For a particle starting far away from the slice, all information about whether the particle would cross the slice during the third or eighth step in the deterministic p = 1 case is lost. Hence, in the longtime dynamics, a particle is equally likely to cross the slice on either step leading to the observed double step structure. We emphasize that this double step structure holds for all $p \neq 1$ (see Fig. 9). However, similar to the Floquet evolution, the flow per full measurement cycle decreases away from 1 for p < 1, as shown in Fig. 6.

VI. AWAY FROM THE ZENO LIMIT

We now turn to consider the important question of whether the flow is still present when the frequency of measurements is reduced; i.e., we study the evolution under

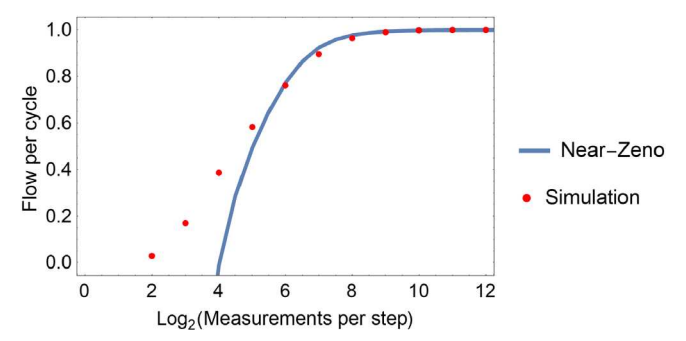


FIG. 10. Flow per cycle as the measurements per step moves away from the Zeno limit. Compared are the values found from the near-Zeno limit approximation, Eq. (30) with the transformation Eq. (42), and the flow found from direct simulation. Both analytics and simulations are done in the perfect switching cycle, i.e., $(T/8) = (\pi/2)$.

our measurement protocol away from the Zeno limit. In Fig. 10 we show the flow as a function of $\log(n)$. We see that the flow is reduced, but still finite as the measurement frequency is reduced, crossing over from near constant behavior at high frequency, to roughly logarithmic behavior, $F \sim 0.2 \log_2(n) - 0.4$ at low frequency n, with $F \sim 0.2$ particles per cycle at n = 8 measurements per step.

The blue line in Fig. 10 represents an analytic perturbative near-Zeno correction which fits the simulations remarkably well for n > 64. To arrive at it, we start with Eq. (15), now retaining terms up to and including order $O(n\tau^2)$. We prove in Appendix G that the resultant evolution, to order $O(n\tau^2)$, can still be completely described in terms of the dynamics of the diagonal of G, with the classically stochastic transfer matrices R_i replaced by the matrices $R_{nz,i}$ given by

$$R_{nz,i} = R_i - n\tau^2 \tilde{R}_i, \tag{42}$$

where \tilde{R}_i is the near-Zeno correction to R_i . As in the Zeno case, we define

$$R_{nz} = R_{nz,8} R_{nz,7} R_{nz,6} R_{nz,5} R_{nz,4} R_{nz,3} R_{nz,2} R_{nz,1}, \qquad (43)$$

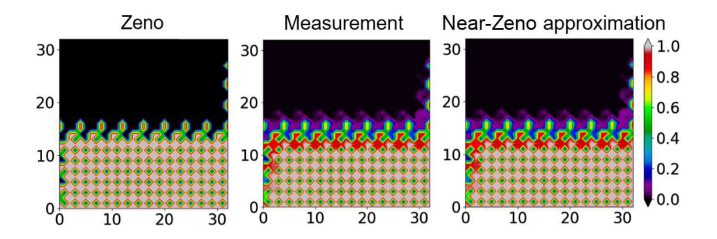


FIG. 11. A comparison of, from left to right, the Zeno limit, the full measurement protocol with 500 measurements per measurement step, and the near-Zeno approximation with 500 measurements per measurement step—all with $(T/8)=(\pi/2)$. Plotted are the local particle densities for a 33 × 33 site Lieb lattice after 51 measurement steps for the lower half filled plane setup given in Fig. 4.

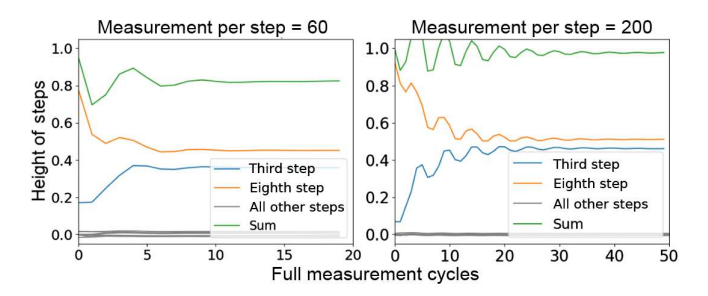


FIG. 12. Flow after each measurement step for n = 60 and n = 200. For both, $(T/8) = (\pi/2)$.

and, in treating R_{nz} , only terms up to $O(n\tau^2)$ are kept after combining Eqs. (42) and (43). Finally, the blue line of Fig. 10 is obtained by substituting Eq. (43) into Eq. (30). In Appendix G, we solve for Eq. (43) explicitly, but here we focus only on the flow resulting from R_{nz} . We also note here that, similar to the Zeno limit case, the flow in the near-Zeno limit is protected to perturbations localized on the boundaries (see Appendix F). Furthermore, numerical simulations suggest that this protection persists even in the low frequency measurement regime. We leave a detailed investigation of this observation to future work.

In Fig. 11 we show what the evolution of density in the system away from the Zeno limit looks like. The main feature is clearly the ability of particles to spread faster into the bulk, since the evolution is not confined as effectively to a sequence of two-site evolution steps as in the Zeno case. We emphasize, however, that there is still significant charge transport even far away from the Zeno regime (Fig. 10). On the other hand, the double step structure is broken with the eighth step in the measurement cycle providing an increasing percentage of the total flow per cycle as the number of measurements per measurement step is reduced. This is shown, for example, in Fig. 12. This is because particles on the edge are less affected by the move away from the Zeno limit (as they have fewer neighboring sites to spread to). Since the eighth measurement step hops across the flow cut at the edge, a larger percentage of the Zeno limit flow is retained.

VII. CONCLUDING REMARKS

In this work we presented a framework for inducing edge modes via measurement protocols. Our work is complementary to the many recent advances in studying time periodic systems such as topological Floquet insulators [1,65]. The resultant behavior is a remarkable demonstration of the role of an observer in quantum mechanics as fundamentally different from a classical observer.

Several remarks are in order regarding open problems. First, we emphasize that the behavior analyzed in this paper is that of the average transport and dynamics of densities over all possible measurement outcomes. While it is

reasonable to expect that such an average would well represent the typical behavior of the system for a typical history of measurement outcomes (a "quantum trajectory"), it is of much interest to study how well this expectation holds by studying both fluctuations and the behavior of the quantum trajectories in our system.

While we have concentrated on the study of the two-point function G, it would also be interesting to establish the limiting behavior of the many-body density matrix ρ as the system is observed. In particular, this would allow us to study the development of entropy and nontrivial correlation in the system. Indeed, in recent works, e.g., Refs. [26–28,43], it has been shown that certain protocols of repeated measurements interspersed with free unitary evolution induce a phase transition in the Rényi entropy dependant on the rate of measurement. In our model, we have found that no two-point correlations are generated up to first order in the expansion away from the Zeno limit, keeping the system close to a product state at all times. However, for low measurement rates, these correlations are clearly generated. This suggests phase transitions of mutual information measures with the measurement rate may be present.

It is important to note that, while in this work we have focused mainly on the Lieb lattice, our procedure may be easily generalized to other lattices. For example, we provide a similar eight-step protocol on a square lattice and a six-step protocol on a "modified" kagome lattice in Appendix C. Furthermore, we describe some restrictions on the kinds of protocols that can be implemented on a given lattice.

We note that while our dynamics is driven by non-interacting evolution, the formalism (see Ref. [46]) allows for an arbitrary initial state, including interesting highly correlated ones. Moreover, we expect that in the Zeno limit, the inclusion of certain interactions may be efficiently implemented with a proper modification of the current treatment, which we leave for future work.

Finally, we suggest that a measurement protocol such as ours, while challenging, may be experimentally realizable. One possibility is the use of quantum dot arrays as the underlying lattice [66]. Another promising direction is quantum gas microscopes. Here, experiments working with ultracold ⁶Li fermions have established the ability to resolve particle presence at single sites; see, e.g., Refs. [67–69].

ACKNOWLEDGMENTS

I. K. would like to thank Kun-Woo Kim for discussions. The work of I. K., B. J. J. K., and M. W. was supported in part by the NSF Grant No. DMR-1918207. G. R. acknowledges support from the Institute of Quantum Information and Matter, an NSF Physics Frontiers Center funded by the Gordon and Betty Moore Foundation, and the Simons Foundation, as well as to the NSF DMR Grant No. 1839271. This work was performed in part at Aspen Center for Physics, which is supported by National Science Foundation Grant No. PHY-1607611.

APPENDIX A: CLOSED HIERARCHY FRAMEWORK

We begin with the most general evolution of a density matrix:

$$\rho \to \mathcal{L}(\rho) = \sum_{\nu} A_{\nu} \rho A_{\nu}^{\dagger}, \qquad \sum_{\nu} A_{\nu}^{\dagger} A_{\nu} = 1. \tag{A1}$$

This form ensures that ρ remains non-negative and the normalization condition on the Krauss operators A_{ν} preserves $\text{Tr}\rho = 1$.

The evolution of a general correlation function,

$$\langle a_{i_1}^{\dagger} ... a_{i_{\ell_1}}^{\dagger} a_{i_{(\ell_1+1)}} ... a_{i_{(\ell_1+\ell_2)}} \rangle = \text{Tr} \rho a_{i_1}^{\dagger} ... a_{i_{\ell_1}}^{\dagger} a_{i_{(\ell_1+1)}} ... a_{i_{(\ell_1+\ell_2)}}, \tag{A2}$$

is given by

$$\langle a_{i_1}^{\dagger}...a_{i_{\ell_1}}^{\dagger}a_{i_{(\ell_1+1)}}...a_{i_{(\ell_1+\ell_2)}}\rangle \rightarrow \langle a_{i_1}^{\dagger}...a_{i_{\ell_1}}^{\dagger}a_{i_{(\ell_1+1)}}...a_{i_{(\ell_1+\ell_2)}}\rangle + \sum_{\nu} \text{Tr}\rho A_{\nu}^{\dagger}[a_{i_1}^{\dagger}...a_{i_{\ell_1}}^{\dagger}a_{i_{(\ell_1+1)}}...a_{i_{(\ell_1+\ell_2)}}, A_{\nu}], \tag{A3}$$

where we have used the normalization condition of A_{ν} . Note that the $\ell_1 + \ell_2$ correlation function is taken to a, in general, higher-order correlation function leading to a hierarchy of equations. A tractable subset of this general evolution can be found by taking the two-point function $G_{ij} \equiv \langle a_i^{\dagger} a_j \rangle$, and asking under what set of Krauss operators does the hierarchy close, i.e., $G \to G' = \mathcal{K}(G)$.

In Ref. [46], it is shown that, for fermions on a lattice, the following Krauss operators form the complete set of all possible operations that close the hierarchy on the two-point function level:

noninteracting evolution:
$$\mathcal{L}_{u}(\rho) = \mathcal{U}\rho\mathcal{U}^{\dagger}$$
, (A4a)

particle detection:
$$\mathcal{L}_{D,i}(\rho) = n_i \rho n_i + (1 - n_i) \rho (1 - n_i),$$
 (A4b)

soft particle injection:
$$\mathcal{L}_{\text{in},i,\epsilon}(\rho) = \epsilon(2-\epsilon)a_i^{\dagger}\rho a_i + [1-\epsilon(1-n_i)]\rho[1-\epsilon(1-n_i)],$$
 (A4c)

soft particle extraction:
$$\mathcal{L}_{\text{out},i,\epsilon}(\rho) = \epsilon(2-\epsilon)a_i\rho a_i^{\dagger} + (1-\epsilon n_i)\rho(1-\epsilon n_i)$$
. (A4d)

Here, \mathcal{U} is assumed to describe noninteracting evolution, under which fermion operators transform as $\mathcal{U}^{\dagger}a_{i}^{\dagger}\mathcal{U} = U_{ij}a_{j}^{\dagger}$, where U is called a single-particle evolution. We have also denoted $n_{i}=a_{i}^{\dagger}a_{i}$ the number operator, and ϵ is a real number between 0 and 1. It is then a straightforward task of applying the anticommutation relations of a^{\dagger} , a to find the corresponding transformations on the two-point function:

noninteracting evolution:
$$\mathcal{K}_U(G)_{ij} = (UGU^{\dagger})_{ij}$$
, (A5a)

particle detection:
$$\mathcal{K}_{D,i}(G) = P_i G P_i + (1 - P_i) G (1 - P_i),$$
 (A5b)

soft particle injection:
$$\mathcal{K}_{\text{in},i,\epsilon}(G) = (1 - P_i)G(1 - P_i) + (1 - \epsilon)P_iG(1 - P_i) + (1 - \epsilon)(1 - P_i)GP_i + (1 - \epsilon)^2P_iGP_i + \epsilon(2 - \epsilon)P_i,$$
 (A5c)

soft particle extraction:
$$\mathcal{K}_{\text{out},i,\epsilon}(G) = \mathcal{K}_{\text{in},i,\epsilon}(G) - \epsilon(2-\epsilon)P_i$$
. (A5d)

Here, $P_i = |i\rangle\langle i|$ is the (single-particle) projector onto site i.

We emphasize that no approximations are used in the derivation of Eq. (A5). The resulting simplicity arises completely from the restricted set of allowed Krauss operations. Equations (A5a) and (A5b) are the starting point for our analysis of the evolution of G in the paper.

APPENDIX B: REMARKS ABOUT STEADY STATES

What kind of steady states can we expect in a system like ours where evolution and density measurements are intertwined? Here it is convenient to look at the steady states of the correlation matrix G rather then the full density matrix ρ . Let us consider how the Hilbert-Schmidt norm of G changes under unitary evolution and measurements Eqs. (A5a) and (A5b) above. The Hilbert-Schmidt norm is defined as

$$||G||_{\mathrm{HS}}^2 \equiv \mathrm{Tr} G^{\dagger} G = \sum_{ij} |G_{ij}|^2. \tag{B1}$$

Clearly, $||G||_{\mathrm{HS}}$ is invariant under unitary evolution of G. Particle measurements of G, as described by Eq. (2), on the other hand, set to zero some of the matrix elements of G and thus can only decrease $||G||_{\mathrm{HS}}$. A necessary (though not sufficient) condition for some G_{steady} to be a steady state of some superoperator Λ , i.e., $\Lambda G_{\mathrm{steady}} = G_{\mathrm{steady}}$, is that the Hilbert-Schmidt norm remains constant. This provides a restriction on Λ . Any particle detection measurement contained in Λ must act trivially, i.e., not eliminate any matrix elements. Thus, without loss of generality writing $\Lambda \equiv \prod_i \Pi_i U_i$ we require that

$$\Lambda G_{\text{steady}} = \prod_{i} \Pi_{i} U_{i} G_{\text{steady}} = \prod_{I} U_{i} G_{\text{steady}}.$$
 (B2)

Note that for our measurement procedure, this is clearly true for any scalar matrix $G_{\rm steady}$. For a $G_{\rm steady}$ with a nonuniform diagonal (such as that of a single localized particle) to be a steady state of the measurement protocol, we can only satisfy Eq. (B2) in the Zeno limit with T/8 fine-tuned to $\pi/2$.

One possibility to find nonequilibrium steady states in the system, as well as offer an insight into larger systems, is to use particle injection and removal as was previously done in Ref. [46]. To stabilize the system where the left half is filled with particles, we may use a strip of width L, where we start where we constantly try to inject particles from the left, and extract any particle that arrives to the right of the sample.

In the context of the present paper, we instead look at the effective behavior of the system, when it is partially filled and evolve over times which are long, but short compared to the time it would take to arrive at the real uniform density steady state.

APPENDIX C: MEASUREMENT PROTOCOL ON OTHER LATTICES

In this appendix, we remark on lattices on which one can perform the measurement protocol outlined above. Our protocol is directly inspired by Floquet cycles where a collection of pairs of neighboring sites are activated at any given step. To mimic this type of dynamics, we require the ability to isolate the activated pairs by performing rapid measurements on neighboring sites. Thus, to apply our protocol directly, we require that there is no hopping amplitude to go between two distinct pairs. For a Hamiltonian describing nearest neighbor hopping on a lattice, this means that the edge distance between unmeasured pairs is at least two (see upper left-hand panel in Fig. 13).

This restriction then rules out the simple cycle on a square lattice originally introduced in Ref. [65], where individual squares are traced out in four steps, as in this case the edge distance between isolated pairs is only one. This does not, however, mean a measurement protocol cannot be implemented on a square lattice. A solution is to increase the size of the cycle to an eight-step process that traces out a path around clusters of four squares (see righthand panel in Fig. 13). Here, the edge distance between activated pairs is 3, and thus they can be isolated using rapid measurements. Note in this example protocol, there is a site at the center of the cycle that is never activated, i.e., always measured. If this site is removed, we find precisely the eight-step protocol on a Lieb lattice introduced in this paper. This choice was made to minimize the number of required measurements and to remove any spreading of particles through these unactivated sites away from the Zeno limit. We also here give an example of another measurement protocol with six measurement steps on a "modified" kagome lattice, as opposed to the eight steps for our protocol on a Lieb lattice, as shown in Fig. 14.

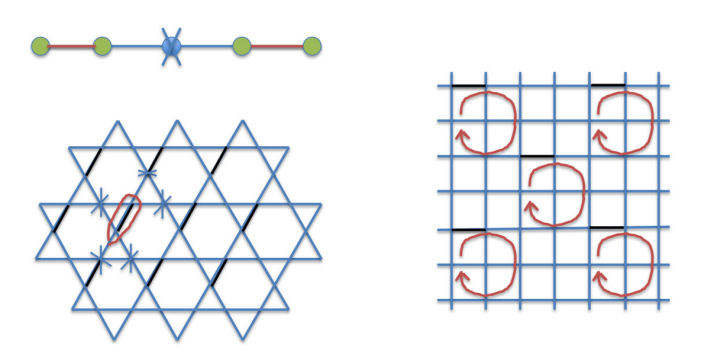


FIG. 13. Upper left: the measurement protocols require the bonds (red) between unmeasured sites (green) to be separated by at least two edges. This allows for at least one measured site (crossed) between them. Lower left: the naive attempt to perform the measurement protocol on the kagome lattice does not work because two of the surrounding measured sites around the unmeasured sites (circled with red) overlap with other unmeasured sites (denoted as the ends of black links). Right: An example of a measurement protocol on a square lattice that satisfies the requirement that the edge distance between unmeasured pairs must be at least 2. If the unactivated (always measured) sites in this protocol are removed, we have exactly the eight-step protocol on a Lieb lattice introduced in this paper.

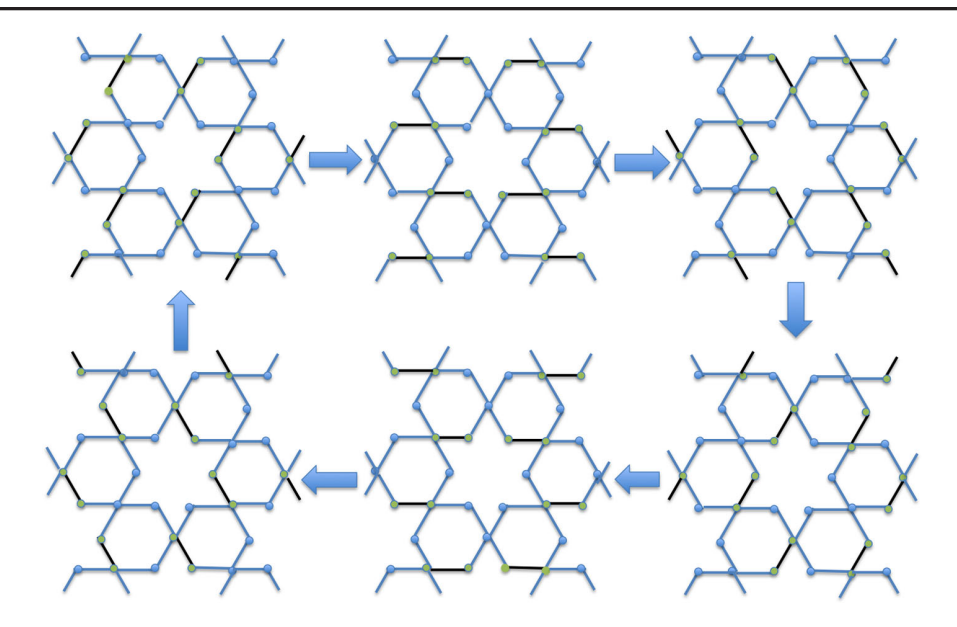


FIG. 14. An example measurement protocol on a "modified" kagome lattice that utilizes six measurement steps (as opposed to the eight-step procedure used on the Lieb lattice). The black bonds indicate free hopping pairs and measurement is indicated by blue colored sites.

APPENDIX D: SOME DERIVATION DETAILS

In this appendix, we supply a few more details about the formulas used in the main text.

(I) Proof of Eq. (7).

$$\prod_{a\in A^c}\pi_a=\sum_{a\in A^c}P_a\otimes P_a+P_A\otimes P_A.$$

We first note that if $a \neq b$, then $p_a p_b = 0$, $p_a (1 - p_b) = p_a$. Thus in the product,

$$\prod_{a \in A^c} \pi_a = \prod_{a \in A^c} [P_a \otimes P_a + (1 - P_a) \otimes (1 - P_a)], \tag{D1}$$

the term of the form $P_a \otimes P_a$ can only appear in a product of the form $(P_a \otimes P_a) \prod_{a' \in A^c; a' \neq a} (1 - P_{a'}) \otimes (1 - P_{a'}) = P_a \otimes P_a$. Next note that $\prod_{a \in A^c} (1 - P_a) = \prod_{a \in A} P_a$. Therefore, $\prod_{a \in A^c} (1 - P_a) \otimes (1 - P_a) = P_A \otimes P_A$. Combining these we get Eq. (7).

(II) Derivation of Eq. (13).

$$\begin{split} \Pi_{A}[H\otimes I-I\otimes H]\Pi_{A} \\ &= \left(\sum_{a\in A^{c}}P_{a}\otimes P_{a} + P_{A}\otimes P_{A}\right)[H\otimes I-I\otimes H]\left(\sum_{b\in A^{c}}P_{b}\otimes P_{b} + P_{A}\otimes P_{A}\right) \\ &= (P_{A}\otimes P_{A})[H\otimes I-I\otimes H](P_{A}\otimes P_{A}) \\ &= H_{A}\otimes P_{A} - P_{A}\otimes H_{A}, \end{split} \tag{D2}$$

where $H_A \equiv P_A H P_A$, and we used that if $a, b \in A^c$, then $P_A P_a = P_A P_b = 0$ and that $P_a P_b = \delta_{ab} P_a$.

APPENDIX E: BULK-EDGE DECOMPOSITION: PROOF OF EQ. (30)

Our starting point is Eq. (26). Taking the ∂_{θ} derivative and using the doubly stochastic nature of $R_{\rm cyc}$ (when $\theta = 0$), i.e., $\langle \mathbf{I} | R_{\rm cyc}(\theta = 0) = \langle \mathbf{I} |$ and $R_{\rm cyc}(\theta = 0) | \mathbf{I} \rangle = | \mathbf{I} \rangle$, we find

$$F_{N} = \frac{1}{NL_{x}} i \partial_{\theta} \chi_{N}(\theta)|_{\theta=0} = \frac{1}{NL_{x}} i \partial_{\theta} \langle \mathbf{I} | R_{\text{cyc}}^{N}(\theta) G | \mathbf{I} \rangle|_{\theta=0} = \frac{1}{NL_{x}} \sum_{m=0}^{N-1} \langle \mathbf{I} | J R_{\text{cyc}}^{m}(\theta=0) G | \mathbf{I} \rangle$$

$$= \frac{1}{NL_{x}} \sum_{m=0}^{N-1} \langle \mathbf{I} | J [R_{\text{cyc}}^{m}(\theta=0), G] | \mathbf{I} \rangle + \frac{1}{L_{x}} \langle \mathbf{I} | J G | \mathbf{I} \rangle, \tag{E1}$$

where we have defined $J=-i\partial_{\theta}R_{\rm cyc}(\theta)|_{\theta=0}$ and G is a diagonal matrix representing the initial density distribution, i.e., if written in matrix elements, $G_{\alpha,\beta}({\bf r},{\bf r}')=\delta_{\alpha\beta}\delta_{{\bf r},{\bf r}'}g_{\alpha}({\bf r})$ with ${\bf r}=(x,y)$ and ${\bf r}'$ coordinates of the unit cell, α,β internal sites, and $g_{\alpha}({\bf r})$ the initial probability for a particle at a site indexed by $({\bf r},\alpha)$. Below we suppress the angle when describing $R_{\rm cyc}(\theta=0)$, and will just write $R_{\rm cyc}$.

In our setup (see Fig. 7), we fill the system in such a way that $g_{\alpha}(\mathbf{r}) = 1$ for $y < \ell_1$ and $g_{\alpha}(\mathbf{r}) = 0$ for $y > \ell_2$. Let us define the set

$$S_m = \{ \mathbf{r} : \ell_1 - m \le y \le \ell_2 + m \}. \tag{E2}$$

The set S_m contains the interface between empty and full region, "thickened" by a height m below and above. Let also P_{S_m} be the projection on the set S_m defined as in Eq. (8). Explicitly,

$$P_{S_m,\alpha,\beta}(\mathbf{r},\mathbf{r}') = \delta_{\alpha\beta}\delta_{\mathbf{r},\mathbf{r}'} \begin{cases} 1 & \ell_1 - m \le y, y' \le \ell_2 + m \\ 0 & \text{otherwise.} \end{cases}$$
(E3)

We now prove that we can freely move the projection P_{S_m} to either side of the commutator $[R^m_{\rm cyc}, G]$; namely, taking the range of $R_{\rm cyc}$ to be short, range $(R_{\rm cyc}) \leq 1$, then

$$[R^m_{\rm cyc},G] = P_{S_m}[R^m_{\rm cyc},G] = [R^m_{\rm cyc},G]P_{S_m} = P_{S_m}[R^m_{\rm cyc},G]P_{S_m}. \eqno(E4)$$

Proof.—Consider the commutator $[R_{\text{cyc}}^m, G]$. Note that since $R_{\alpha\beta}(\mathbf{r}, \mathbf{r}') = 0$ if $|\mathbf{r} - \mathbf{r}'| > 1$, we have $R_{\alpha\beta}^m(\mathbf{r}, \mathbf{r}') = 0$

if $|\mathbf{r} - \mathbf{r}'| > m$. Therefore, looking at the matrix elements, we have $([R^m_{\rm cyc}, G])_{\alpha\beta}(\mathbf{r}, \mathbf{r}') = R^m_{\alpha\beta}(\mathbf{r}, \mathbf{r}')[g_\beta(\mathbf{r}') - g_\alpha(\mathbf{r})] = 0$ when $|\mathbf{r} - \mathbf{r}'| > m$ or $g_\beta(\mathbf{r}') - g_\alpha(\mathbf{r}) = 0$. Thus, the matrix elements of $[R^m_{\rm cyc}, G]$ can only be nonzero when simultaneously $|\mathbf{r} - \mathbf{r}'| \le m$ and $g_\beta(\mathbf{r}') - g_\alpha(\mathbf{r}) \ne 0$. Let us check when the matrix elements can be nonvanishing.

Since the system is filled in such a way that $g_{\alpha}(\mathbf{r}) = 1$ for $y < \ell_1$, we see that if $y < \ell_1 - m$, the condition that $|\mathbf{r} - \mathbf{r}'| \le m$ implies $y' \le \ell_1$, and in particular $g_{\beta}(\mathbf{r}') = g_{\alpha}(\mathbf{r}) = 1$, making the commutator vanish. Similarly, the commutator will vanish if $y > \ell_2 + m$. And of course the same considerations can be applied to y'. We conclude that nonzero matrix elements are only possible if

$$\ell_1 - m \le y, \qquad y' \le \ell_2 + m, \tag{E5}$$

which implies Eq. (E4).

Since the boundaries of the system are not included in the S_m region, we may also replace the open boundary conditions of R_{cyc}^m with periodic ones, denoted by R_B^m , to get

$$[R_{\text{cvc}}^m, G] = P_{S_m}[R_{\text{cvc}}^m, G] = [R_R^m, G]P_{S_m}.$$
 (E6)

Similarly, since J is short-ranged, far from the boundaries, the matrix elements of J are identical to those of $J_B\!\equiv\!-i\partial_\theta R_B(\theta)|_{\theta=0}$; namely, $JP_{S_m}=J_BP_{S_m}$. This behavior holds when $m<\min[\ell_1-\mathrm{range}(J),L_y-\ell_2-\mathrm{range}(J)]$, which will always be assumed in the following treatment. Thus, we have

$$\langle \mathbf{I}|J[R_{\text{cyc}}^m, G]|\mathbf{I}\rangle = \langle \mathbf{I}|JP_{S_m}[R_{\text{cyc}}^m, G]|\mathbf{I}\rangle = \langle \mathbf{I}|J_BP_{S_m}[R_B^m, G]|\mathbf{I}\rangle. \tag{E7}$$

Substituting in Eq. (E1), we get

$$\begin{split} F_{N} &= \frac{1}{NL_{x}} \sum_{m=0}^{N-1} \langle \mathbf{I} | J_{B} P_{S_{m}}[R_{B}^{m}, G] | \mathbf{I} \rangle + \frac{1}{L_{x}} \langle \mathbf{I} | JG | \mathbf{I} \rangle \\ &= \frac{1}{NL_{x}} \sum_{m=0}^{N-1} \langle \mathbf{I} | J_{B} P_{S_{m}} R_{B}^{m} G | \mathbf{I} \rangle - \frac{1}{NL_{x}} \sum_{m=0}^{N-1} \langle \mathbf{I} | J_{B} P_{S_{m}} G | \mathbf{I} \rangle + \frac{1}{L_{x}} \langle \mathbf{I} | JG | \mathbf{I} \rangle \\ &= \frac{1}{NL_{x}} \sum_{m=0}^{N-1} \langle \mathbf{I} | J_{B} P_{S_{m}} R_{B}^{m} G | \mathbf{I} \rangle + \frac{1}{NL_{x}} \sum_{m=0}^{N-1} \langle \mathbf{I} | J(G - P_{S_{m}} G) | \mathbf{I} \rangle, \end{split} \tag{E8}$$

where in the last line we used that in the bulk $\langle \mathbf{I}|J_BP_{S_m}G|\mathbf{I}\rangle = \langle \mathbf{I}|JP_{S_m}G|\mathbf{I}\rangle$.

To proceed we note that

$$G - P_{S_m}G = (1 - P_{S_m})G = (P_{y < \ell_1 - m} + P_{y > \ell_2 + m})G = P_{y < \ell_1 - m}, \tag{E9}$$

where $P_{y<\ell_1-m}$, $P_{y>\ell_2+m}$ are projectors onto the regions with y below $y=\ell_1-m$ and y above $y=\ell_2+m$, respectively. Also, we used that $P_{y<\ell_1-m}G=P_{y<\ell_1-m}$ and $P_{y<\ell_2+m}G=0$, which follow immediately from the definition of G. Therefore,

$$F_{N} = \frac{1}{NL_{x}} \sum_{m=0}^{N-1} \langle \mathbf{I} | J_{B} P_{S_{m}} R_{B}^{m} G | \mathbf{I} \rangle + \frac{1}{NL_{x}} \sum_{m=0}^{N-1} \langle \mathbf{I} | J P_{y < \ell_{1} - m} | \mathbf{I} \rangle.$$
(E10)

We can further simplify as follows. Let us assume there is no bulk current per unit cell. Then, if averaged over a bulk strip whose width is a unit cell, we have $\langle \mathbf{I}|J(P_{y<\ell_1-m}-P_{y<\ell_1-(m-1)})|\mathbf{I}\rangle=0$, which, finally, taking range(J) = 1, yields the form

$$\begin{split} F_{N} &= \frac{1}{NL_{x}} \sum_{m=0}^{N-1} \langle \mathbf{I} | J_{B} P_{S_{m}} R_{B}^{m} G | \mathbf{I} \rangle + \frac{1}{L_{x}} \langle \mathbf{I} | J P_{y \leq 2} | \mathbf{I} \rangle \\ &\equiv F_{\text{bulk}} + F_{\text{edge}}. \end{split} \tag{E11}$$

In other words, we have split the charge transport into a term that depends only on the bulk properties of the system,

$$F_{\text{bulk}} = \frac{1}{NL_{x}} \sum_{m=0}^{N-1} \langle \mathbf{I} | J_{B} P_{S_{m}} R_{B}^{m} G | \mathbf{I} \rangle, \qquad (E12)$$

and a term that can be computed near the edge,

$$F_{\text{edge}} = \frac{1}{L_x} \langle \mathbf{I} | J P_{y \le 2} | \mathbf{I} \rangle. \tag{E13}$$

Let us consider the two terms separately.

Edge term F_{edge} .—We can efficiently compute $\langle \mathbf{I}|JP_{y\leq 2}|\mathbf{I}\rangle$, which can be done explicitly by writing the transition matrix for a ladder geometry of small extension in the y direction. Note that due to the short-range nature of J, the edge expression can be further reduced to $\langle \mathbf{I}|P_{y\leq 3}JP_{y\leq 2}|\mathbf{I}\rangle$.

Doing so for our system on *Mathematica* we find with our measurement protocol $F_{\text{edge}} = p^2 + p^3 + p^4$.

Bulk term F_{bulk} .—Assuming the translational invariance of R_B , we can write F_{bulk} expressed in k space by defining the momentum states,

$$|\mathbf{k}\rangle_{\alpha} = \frac{1}{\sqrt{V}} \sum_{\mathbf{r}} e^{i\mathbf{k}\cdot\mathbf{r}} |\mathbf{r}, \alpha\rangle, \qquad |\mathbf{r}, \alpha\rangle = \int \frac{d^2k}{(2\pi)^2} e^{-i\mathbf{k}\cdot\mathbf{r}} |\mathbf{k}\rangle_{\alpha},$$
(E14)

where $V = L_x L_y$ is the number of unit cells. To proceed, let us write the uniform density vector $|\mathbf{I}\rangle$ as

$$|\mathbf{I}\rangle = \sum_{\mathbf{r},\alpha} |\mathbf{r},\alpha\rangle = \sqrt{V} \sum_{\alpha} |\mathbf{k} = 0\rangle_{\alpha}.$$
 (E15)

Therefore, using the momentum representation in Eq. (E12) we arrive at

$$F_{\text{bulk}} = \frac{V}{NL_x} \sum_{m=0}^{N-1} \sum_{\alpha\beta} (J_B)_{\alpha\gamma} (\langle \mathbf{k} = 0 | P_{S_m} R_B^m G | \mathbf{k} = 0 \rangle)_{\gamma\beta}.$$
(E16)

To evaluate this expression, we need, explicitly,

$$\langle k_x = 0, k_y |_{\alpha} G | k_x' = 0, k_y' \rangle_{\beta} = \frac{\delta_{\alpha\beta}}{L_y} \sum_{y} g_{\alpha}(y) e^{-iy(k_y - k_y')},$$
(E17)

where $g_{\alpha}(y) = L_x^{-1} \sum_{x} g_{\alpha}(\mathbf{r})$. For the evolution, let us write R_R^m in the form

$$\langle k_x = 0, k_y |_{\alpha} R_B^m | k_x' = 0, k_y' \rangle_{\beta} = \delta_{k_x k_x'} \delta_{k_y k_y'} \sum_{v=-m}^m C_{\alpha\beta m v} e^{ik_y v},$$
(E18)

where the coefficients $C_{\alpha\beta mv}$ depend on the model. The restriction $-m \le v \le m$ follows from the range of R_B^m being limited to m. Also note that

$$\langle \mathbf{k} |_{\alpha} P_{S_m} | \mathbf{k}' \rangle_{\beta} = \frac{\delta_{\alpha\beta} \delta_{k_x k_x'}}{L_y} \sum_{\ell_1 - m \le y \le \ell_2 + m} e^{-iy(k_y - k_y')}. \quad (E19)$$

Putting these together, we have

$$(\langle \mathbf{k} = 0 | P_{S_m} R_B^m G | \mathbf{k} = 0 \rangle)_{\alpha\beta} = \frac{1}{L_y} \int \frac{dk_y'}{2\pi} \sum_{\ell_1 - m \le y \le \ell_2 + m} e^{ik_y'y} \sum_{v = -m}^m C_{\alpha\beta mv} e^{ik_y'v} \sum_{y'} g_{\beta}(y') e^{-ik_y'y'}$$

$$= \frac{1}{L_y} \sum_{\ell_1 - m \le y \le \ell_2 + m} \sum_{y'} \sum_{v = -m}^m C_{\alpha\beta mv} \left(\int \frac{dk_y'}{2\pi} e^{ik_y'(y - y' + v)} \right) g_{\beta}(y')$$

$$= \frac{1}{L_y} \sum_{v = -m}^m C_{\alpha\beta mv} \sum_{\ell_1 - m \le y \le \ell_2 + m} g_{\beta}(y + v)$$

$$= \frac{1}{L_y} \sum_{v = -m}^m C_{\alpha\beta mv} \sum_{\ell_1 - m + v \le y \le \ell_2 + m + v} g_{\beta}(y)$$

$$= \frac{1}{L_y} \sum_{v = -m}^m C_{\alpha\beta mv} \left[\left(\sum_{y = \ell_1}^{\ell_2} g_{\beta}(y) + m \right) - v \right]$$

$$= \frac{1}{L_y} \left[i\partial_{k_y} [R_B^m(\mathbf{k})]_{\alpha\beta} + \left(\sum_{v = \ell_1}^{\ell_2} g_{\beta}(y) + m \right) [R_B^m(\mathbf{k})]_{\alpha\beta} \right]_{\mathbf{k} = \mathbf{0}}.$$
(E20)

Therefore, we have

$$F_{\text{bulk}} = \frac{V}{NL_{x}} \sum_{m=0}^{N-1} \sum_{\alpha\beta\gamma} (J_{B})_{\alpha\gamma} (\langle \mathbf{k} = 0 | P_{S_{m}} R_{B}^{m} G | \mathbf{k} = 0 \rangle)_{\gamma\beta}$$

$$= \frac{1}{N} \sum_{m=0}^{N-1} \sum_{\alpha\beta} \left\{ i [J_{B}(\mathbf{k}) \partial_{k_{y}} (R_{B}^{m}(\mathbf{k}))]_{\alpha\beta} |_{\mathbf{k}=0} + \left(\sum_{y=\ell_{1}}^{\ell_{2}} g_{\beta}(y) + m \right) [J_{B}(\mathbf{k}) (R_{B}^{m}(\mathbf{k}))]_{\alpha\beta} |_{\mathbf{k}=0} \right\}. \tag{E21}$$

Next, we note that in Eq. (E21) above, we can use

$$\sum_{\alpha\beta} m[J_B(\mathbf{k})(R_B^m(\mathbf{k}))]_{\alpha\beta}|_{\mathbf{k}=0} = 0.$$
 (E22)

This follows from the fact that R_B is a stochastic matrix, with $R_B|\mathbf{I}\rangle = |\mathbf{I}\rangle$, and the assumption that there is no net current in the uniform density system:

$$0 = \langle \mathbf{I} | J_B | \mathbf{I} \rangle = \langle \mathbf{I} | J_B R_B^m | \mathbf{I} \rangle = V \sum_{\alpha \beta} [J_B(\mathbf{k}) (R_B^m(\mathbf{k}))]_{\alpha \beta}|_{\mathbf{k} = 0} = 0.$$
 (E23)

Let us define $c_{\alpha} \equiv \sum_{y=\ell_1}^{\ell_2} g_{\alpha}(y)$. We then have

$$F_{\text{bulk}} = \frac{1}{N} \sum_{m=0}^{N-1} \sum_{\alpha\beta} \left\{ i [J_B(\mathbf{k}) \partial_{k_y} (R_B^m(\mathbf{k}))]_{\alpha\beta} |_{\mathbf{k}=0} + [J_B(\mathbf{k}) (R_B^m(\mathbf{k}))]_{\alpha\beta} c_{\beta} |_{\mathbf{k}=0} \right\}. \tag{E24}$$

Now, using repeatedly that $R_B|\mathbf{I}\rangle = |\mathbf{I}\rangle$, we write

$$\frac{1}{N} \sum_{m=0}^{N-1} \sum_{\alpha\beta} \left\{ i \left[J_{B}(\mathbf{k}) \partial_{k_{y}} (R_{B}^{m}(\mathbf{k})) \right]_{\alpha\beta} \Big|_{\mathbf{k}=0} + \left[J_{B}(\mathbf{k}) (R_{B}^{m}(\mathbf{k})) \right]_{\alpha\beta} c_{\beta} \Big|_{\mathbf{k}=0} \right\}$$

$$= \frac{i}{N} \sum_{m=1}^{N-1} \sum_{\alpha\beta} \left\{ \left[J_{B}(\mathbf{k}) \sum_{q=0}^{m-1} R_{B}^{q}(\mathbf{k}) \partial_{k_{y}} R_{B}(\mathbf{k}) \right]_{\alpha\beta} \Big|_{\mathbf{k}=0} + \left[J_{B}(\mathbf{k}) \frac{R_{B}(\mathbf{k})^{N} - I}{R_{B}(\mathbf{k}) - I} \right]_{\alpha\beta} c_{\beta} \Big|_{\mathbf{k}=0} \right\}$$

$$= \frac{1}{N} \sum_{\alpha\beta} \left\{ i \left[J_{B}(\mathbf{k}) \left(\frac{N[I - R_{B}(\mathbf{k})] + R_{B}^{N}(\mathbf{k}) - I}{[I - R_{B}(\mathbf{k})]^{2}} \right) \partial_{k_{y}} R_{B}(\mathbf{k}) \right]_{\alpha\beta} \Big|_{\mathbf{k}=0} + \left[J_{B}(\mathbf{k}) \frac{R_{B}(\mathbf{k})^{N} - I}{R_{B}(\mathbf{k}) - I} \right]_{\alpha\beta} c_{\beta} \Big|_{\mathbf{k}=0} \right\}. \quad (E25)$$

We now consider the large N limit. If we assume that c_{β} does not scale with N, the dominant term becomes

$$F_{\text{bulk}} = i \sum_{\alpha\beta} \left[J_B(\mathbf{k}) \frac{1}{I - R_B(\mathbf{k})} \partial_{k_y} R_B(\mathbf{k}) \right]_{\alpha\beta} \Big|_{\mathbf{k} = 0}, \quad (E26)$$

which is Eq. (31).

APPENDIX F: ROBUSTNESS OF FLOW

In this appendix, we show that the results of Appendix E are robust to perturbations near the boundary (see Fig. 15). Consider a perturbation of our stochastic dynamics $R_{\rm cyc}$, affecting regions away from the bulk of the sample where we have our interface between the occupied and unoccupied regions. Let us take it as described by a modified dynamics given by R_M of the form:

$$R_{M}(\mathbf{r},\mathbf{r}') = \begin{cases} \tilde{R} & r_{y}, r_{y}' \leq \ell_{1} - (N+1) \\ R_{\text{cyc}} & \ell_{1} - (N+1) \leq r_{y}, r_{y}' \leq \ell_{2} + (N+1) \\ \tilde{R}' & r_{y}, r_{y}' \geq \ell_{2} + (N+1) \\ 0 & \text{otherwise,} \end{cases}$$
(F1)

where \tilde{R}, \tilde{R}' are real matrices such that R_M is doubly stochastic; i.e., R_M is identical to $R_{\rm cyc}$ in the bulk but modified near the boundary. We now calculate the flow for

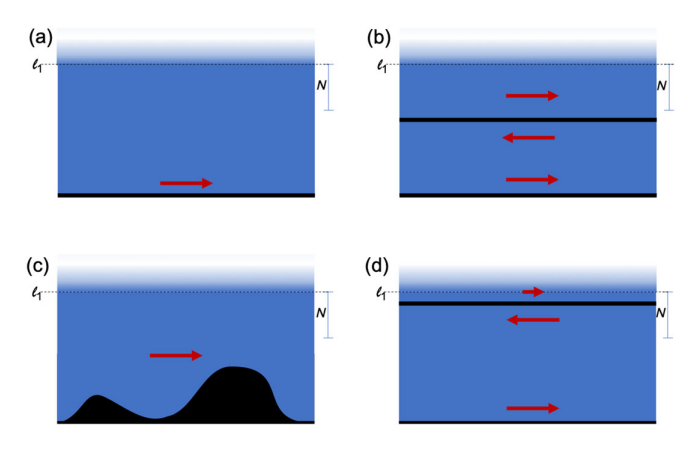


FIG. 15. An illustration of the stability of the flow. When the initial state has uniform density below the line ℓ_1 , our N cycle flow is only sensitive to perturbations occurring in the region above $\ell_1 - N$. For large N, the initial density configurations (a), (b), and (c) will have the same N cycle transport despite having drastic differences in R matrices (e.g., by introducing new edges in the system drawn in black above). On the other hand, panel (d) will have a reduced N cycle flow, since, in contrast with panel (b), the partially filled area on the upper part of the new edge will not be enough to cancel the flow below it.

this new matrix R_M and show it is equivalent to that of R_{cyc} . The situation is illustrated in Fig. 15.

Following Eq. (E1), we find the flow for R_M is

$$F_N = \frac{1}{NL_x} i\partial_\theta \langle \mathbf{I} | R_M^N(\theta) G | \mathbf{I} \rangle, \tag{F2}$$

where we have added the counting field such that $[R_M(\theta)]_{\alpha\beta} = [R_M]_{\alpha\beta}e^{-i(\beta_x-\alpha_x)\theta}$ with $\alpha=(\alpha_x,\alpha_y)$ and $\beta=(\beta_x,\beta_y)$. Defining a matrix which is only modified in the bottom edge,

$$R'_{M}(\mathbf{r}, \mathbf{r}') = \begin{cases} \tilde{R} & r_{y}, r'_{y} \leq \ell_{1} - (N+1) \\ R_{\text{cyc}} & r_{y}, r'_{y} \geq \ell_{1} - (N+1) \\ 0 & \text{otherwise,} \end{cases}$$
(F3)

we note that

$$R_M^N G = R_M^{\prime N} G. \tag{F4}$$

This is because the only nonzero contributions to $R_M^N G$ come from terms at $r_y, r_y' \le \ell_2 + N$; hence, we are free to replace $\tilde{R}' \to R_{\rm cyc}$ in the region $r_y, r_y' > \ell_2 + N$ without changing the result. Combining Eq. (F2) with Eq. (F4) and following the rest of the steps in Eq. (E1), we find

$$F_{N} = \frac{1}{NL_{x}} \sum_{m=0}^{N-1} \langle \mathbf{I} | J_{M}'[R_{M}^{\prime m}(\theta=0), G] | \mathbf{I} \rangle + \frac{1}{L_{x}} \langle \mathbf{I} | J_{M}'G | \mathbf{I} \rangle,$$
(F5)

where J'_M is the current associated with R'_M . Similar to Eq. (E4), we find

$$[R_M^{\prime m}(\theta=0), G] = [R_M^{\prime m}(\theta=0), G]P_S$$
 (F6)

Note that in the region S_m , R_M' is identical to $R_{\rm cyc}$. We therefore have

$$\begin{split} [R_{M}^{\prime m}(\theta=0),G]P_{S_{m}} &= [R_{\text{cyc}}^{m}(\theta=0),G]P_{S_{m}} \\ &= [R_{B}^{m}(\theta=0),G]P_{S_{m}}. \end{split} \tag{F7}$$

Repeating the steps that led to Eq. (E10), we find

$$F_{N} = \frac{1}{NL_{x}} \sum_{m=0}^{N-1} \langle \mathbf{I} | J_{B} P_{S_{m}} R_{B}^{m} G | \mathbf{I} \rangle$$

$$+ \frac{1}{NL_{x}} \sum_{m=0}^{N-1} \langle \mathbf{I} | J_{M}^{\prime} P_{y < \ell_{1} - m} | \mathbf{I} \rangle. \tag{F8}$$

Note that the first term in Eq. (F8) is equivalent to the F_{bulk} contribution for R_{cyc} . We now show that $(1/NL_x)\sum_{m=0}^{N-1} \times \langle \mathbf{I}|J_M'P_{y<\ell_1-m}|\mathbf{I}\rangle$ is equivalent to the F_{edge} contribution from R_{cvc} .

Note,

$$\frac{1}{NL_{x}} \sum_{m=0}^{N-1} \langle \mathbf{I} | J'_{M} P_{y < \ell_{1} - m} | \mathbf{I} \rangle = \frac{1}{NL_{x}} \sum_{m=0}^{N-1} \langle \mathbf{I} | J'_{M} P_{\ell_{1} - N + m > y > \ell_{1} - N} | \mathbf{I} \rangle + \frac{1}{L_{x}} \langle \mathbf{I} | J'_{M} P_{y < \ell_{1} - N} | \mathbf{I} \rangle$$

$$= \frac{1}{NL_{x}} \sum_{m=0}^{N-1} \langle \mathbf{I} | J P_{\ell_{1} - N + m > y > \ell_{1} - N} | \mathbf{I} \rangle + \frac{1}{L_{x}} \langle \mathbf{I} | J'_{M} P_{y < \ell_{1} - N} | \mathbf{I} \rangle$$

$$= \frac{1}{L_{x}} \langle \mathbf{I} | J'_{M} P_{y < \ell_{1} - N} | \mathbf{I} \rangle, \tag{F9}$$

where in the second and third lines we have used the fact that J_M' is identical to J for $y > \ell_1 - N$ and that $R_{\rm cyc}$ has no bulk transport implies $\langle \mathbf{I} | J P_{\ell_1 - N + m > y > \ell_1 - N} | \mathbf{I} \rangle = 0$. Furthermore.

$$\frac{1}{L_x} \langle \mathbf{I} | J_M' P_{y < \ell_1 - N} | \mathbf{I} \rangle = \frac{1}{L_x} \langle \mathbf{I} | J_M' (I - P_{y > \ell_1 - N}) | \mathbf{I} \rangle. \quad (F10)$$

We now restrict ourselves to the case where $\langle \mathbf{I} | \mathbf{J}_M' | \mathbf{I} \rangle = 0$, i.e., no net current in the uniform density state. Note that this is the case when R is a product of bistochastic symmetric matrices, which includes many of the most natural perturbations near the boundary (random potentials, removed sites, variation in hopping amplitude or measurement step timing, etc.). In this case, we find

$$\begin{split} \frac{1}{L_{x}}\langle\mathbf{I}|J'_{M}(I-P_{y>\ell_{1}-N})|\mathbf{I}\rangle &= -\frac{1}{L_{x}}\langle\mathbf{I}|J'_{M}P_{y>\ell_{1}-N}|\mathbf{I}\rangle = -\frac{1}{L_{x}}\langle\mathbf{I}|JP_{y>\ell_{1}-N}|\mathbf{I}\rangle \\ &= \frac{1}{L_{x}}\langle\mathbf{I}|JP_{y\leq2}|\mathbf{I}\rangle = F_{\text{edge}}. \end{split} \tag{F11}$$

We thus have that flow is unaffected by arbitrary evolution near the boundary. It is only dependent on the bulk properties of the evolution. Note this argument also holds if $R_{\rm cyc}$ is replaced by R_{nz} , the dynamics in the near-Zeno case. In other words, transport is completely protected even (to first order) away from the Zeno limit. In fact, numerical simulations suggest that edge transport is unaffected by perturbations near the boundary even in the low frequency measurement regime. Proof of this, however, is still a work in progress.

APPENDIX G: NEAR-ZENO APPROXIMATION: DERIVATION OF R_{nz}

Our starting point is Eq. (12). Let us now include terms of order up to $O(\tau^2)$, and rewrite it as

$$\Pi_{A_{i}}(U \otimes \bar{U})\Pi_{A_{i}} = \Pi_{A_{i}} - i\tau[H_{A_{i}} \otimes P_{A_{i}} - P_{A_{i}} \otimes H_{A_{i}}] - \frac{\tau^{2}}{2}\Pi_{A_{i}}[H \otimes I - I \otimes H]^{2}\Pi_{A_{i}} + O(\tau^{3})$$

$$= \Pi_{A_{i}}(U_{A_{i}} \otimes \bar{U}_{A_{i}})\Pi_{A_{i}} - \tau^{2}\zeta_{A_{i}}(H) + O(\tau^{3}), \tag{G1}$$

where

$$\zeta_{A_i}(H) = \frac{1}{2} \Pi_{A_i} [H^2 \otimes I + I \otimes H^2 - 2H \otimes H] \Pi_{A_i} - \frac{1}{2} [H_{A_i}^2 \otimes P_{A_i} + P_{A_i} \otimes H_{A_i}^2 - 2H_{A_i} \otimes H_{A_i}]. \tag{G2}$$

From this we find

$$\begin{split} \Pi_{A_{i+1}}[\Pi_{A_i}(U \otimes \bar{U})\Pi_{A_i}]^n\Pi_{A_{i-1}} &= \Pi_{A_{i+1}}[\Pi_{A_i}(U_{A_i} \otimes \bar{U}_{A_i})\Pi_{A_i} - \tau^2\zeta_{A_i}(H)]^n\Pi_{A_{i-1}} + O(n\tau^3) \\ &= \Pi_{A_i \cap A_{i+1}}(U_{A_i}^n \otimes \bar{U}_{A_i}^n)\Pi_{A_i \cap A_{i-1}} - \tau^2\Pi_{A_i \cap A_{i+1}} \sum_{m=0}^{n-1}(U_{A_i}^m \otimes \bar{U}_{A_i}^m)\zeta_{A_i}(H) \\ &\qquad \times (U_{A_i}^{n-1-m} \otimes \bar{U}_{A_i}^{n-1-m})\Pi_{A_i \cap A_{i-1}} + O(\tau^3 n). \end{split}$$

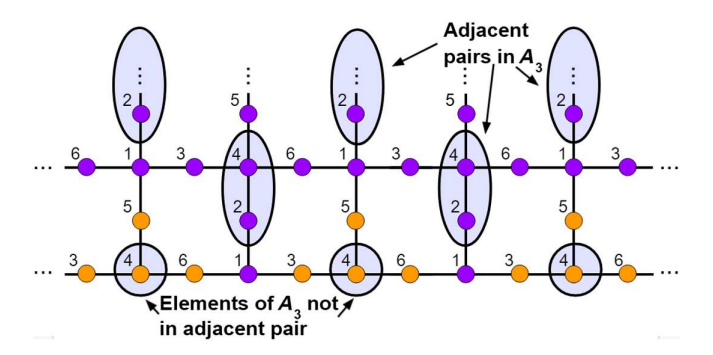


FIG. 16. For any given A_i , here we take without loss of generality i=3, some elements of A_i have a neighbor also in A_i . Other sites in A_i have no such nearest neighbor. As described in Appendix G, all sites evolve in the near-Zeno approximation in one of two ways. Lone sites in A_i and nearest neighbors to lone sites in A_i (as shown in orange) exhibit an evolution given by case 1 of the near-Zeno term of Eq. (G3). However, the evolution for sites that are in an adjacent pair in A_i or neighboring an adjacent pair in A_i (shown in purple) are governed by case 2.

The first term in Eq. (G3) corresponds to the evolution in the Zeno limit and generates the operation R_i on the diagonal of G (as is explained in the Zeno limit Sec. IV). The second term, as will be shown, corresponds to the \tilde{R}_i operations on the diagonal of G.

To see this, we start by noting that the operator $\Pi_{A_i \cap A_{i+1}}$ kills the correlations between every pair of sites, unless both sites are within $A_i \cap A_{i+1}$. Hence, off-diagonal elements of G are only generated if $(U_{A_i}^m \otimes \bar{U}_{A_i}^m)\zeta_{A_i}(H)(U_{A_i}^{n-1-m} \otimes \bar{U}_{A_i}^{m-1-m})$ can generate correlations between the elements of $A_i \cap A_{i+1}$. The operators $(U_{A_i} \otimes \bar{U}_{A_i})$ can only generate correlations within the neighboring pairs inside of A_i . Now, note that the neighboring pairs within A_i are separated by at

least three edges. Therefore, to generate correlations between the neighboring pairs using a power of H, i.e., H^{ν} , we must have at least $\nu \geq 3$. $\zeta_{A_i}(H)$, on the other hand, contains H with a power of at most 2. It follows then that neither $\zeta_{A_i}(H)$ nor $(U_{A_i} \otimes \bar{U}_{A_i})$ can generate correlations between the adjacent pairs in A_i . Hence, any correlations generated by $(U_{A_i}^m \otimes \bar{U}_{A_i}^m)\zeta_{A_i}(H)(U_{A_i}^{n-1-m} \otimes \bar{U}_{A_i}^{n-1-m})$ will be subsequently killed by $\Pi_{A_i \cap A_{i+1}}$. We thus again have that the evolution of G may be described fully by the dynamics of the diagonal of G. Furthermore, we may replace $\Pi_{A_i \cap A_{i+1}}$ in Eq. (G3) with an operator that simply kills all correlations, namely, $\sum_a P_a \otimes P_a$.

At this point in the analysis, there are two cases for the action of $(U_{A_i} \otimes \bar{U}_{A_i})$ which we now consider. For sites in A_i^c and for sites in A_i without a neighboring site also in A_i (see Fig. 16), $(U_{A_i} \otimes \bar{U}_{A_i})$ simply acts as an identity. On the other hand, for sites in A_i with a neighboring site also in A_i , $(U_{A_i} \otimes \bar{U}_{A_i})$ will induce Rabi oscillations within the neighboring pair inside of A_i .

We further note that, for any given site b, the near-Zeno term in Eq. (G3) only induces an interaction between b, the closest element or pair in A_i to b, and other nearest neighbors to this element or pair in A_i (see Fig. 16). This is by nature of the fact that the $H^2 \otimes I$ and $I \otimes H^2$ terms (the only terms that act nontrivially on sites outside of A_i) in $\zeta_{A_i}(H)$ are sandwiched by Π_{A_i} , and so can only affect nearest neighbors to any given element of A_i . We therefore find that we have two disjoint sets of sites, as given in Fig. 16, that are affected by the near-Zeno term in Eq. (G3) differently.

Case 1.—Here (orange sites in Fig. 16), the second term in Eq. (G3) becomes

$$-\tau^2 \sum_a (P_a \otimes P_a) \sum_{m=0}^{n-1} \zeta_{A_i}(H) \sum_b (P_b \otimes P_b) = -n\tau^2 \sum_{a,b} (P_a \otimes P_a) \zeta_{A_i}(H) (P_b \otimes P_b). \tag{G4}$$

We now simplify to find

$$\sum_{a,b} (P_a \otimes P_a) \zeta_{A_i}(H) (P_b \otimes P_b) = \sum_{a,b} (P_a \otimes P_a) \left\{ \frac{1}{2} \Pi_{A_i} [H^2 \otimes I + I \otimes H^2 - 2H \otimes H] \Pi_{A_i} - \frac{1}{2} [H_{A_i}^2 \otimes P_{A_i} + P_{A_i} \otimes H_{A_i}^2 - 2H_{A_i} \otimes H_{A_i}] \right\} (P_b \otimes P_b)$$

$$= \sum_a \deg(a) (P_a \otimes P_a) - \sum_{a,b} P_a H P_b \otimes P_a H P_b, \tag{G5}$$

where we have used the fact that $H_{A_i} = P_{A_i} H P_{A_i} = 0$ since in case 1 no element of A_i has a nearest neighbor also in A_i . This implies that \tilde{R}_i is given by

case 1:
$$[\tilde{R}_i]_{ab} = \begin{cases} \deg(a) & \text{for } a = b \\ -1 & \text{for } a, b \text{ nearest neighbors} \\ 0 & \text{otherwise.} \end{cases}$$
 (G6)

Case 2.—Here (purple sites in Fig. 16), note that $U_{A_i} \otimes \bar{U}_{A_i} = e^{-i\tau O}$, where we have defined

$$O \equiv H_{A_i} \otimes P_{A_i} - P_{A_i} \otimes H_{A_i}. \tag{G7}$$

Furthermore, the following relations hold,

$$O^2 = 2(P_{A_i} \otimes P_{A_i} - H_{A_i} \otimes H_{A_i}) \equiv 2E, \tag{G8}$$

$$OE = 2O,$$
 (G9)

where we have defined E in the first line and used the fact that H_{A_i} simply acts like the Pauli matrix σ_x for nearest neighbors in the subspace A_i , i.e., $H_{A_i}^2 = P_A$.

It then follows that

$$U_{A_i} \otimes \bar{U}_{A_i} = e^{-i\tau O} = \left(\frac{E}{2} - \frac{E}{2}\right) + 1 - 2i\tau \frac{O}{2} - (2\tau)^2 \frac{E}{2} + \frac{i}{3!} (2\tau)^3 \frac{O}{2} + \cdots$$

$$= \left(1 - \frac{E}{2}\right) + \frac{E}{2}\cos 2\tau - i\frac{O}{2}\sin 2\tau. \tag{G10}$$

We therefore find

$$\begin{split} &\sum_{m=0}^{n-1} (U_{A_{i}}^{m} \otimes \bar{U}_{A_{i}}^{m}) \zeta_{A_{i}}(H) (U_{A_{i}}^{n-1-m} \otimes \bar{U}_{A_{i}}^{n-1-m}) \\ &= \sum_{m=0}^{n-1} \left[\left(1 - \frac{E}{2} \right) + \frac{E}{2} \cos 2m\tau - i \frac{O}{2} \sin 2m\tau \right] \zeta_{A_{i}}(H) \left[\left(1 - \frac{E}{2} \right) + \frac{E}{2} \cos 2m\tau + i \frac{O}{2} \sin 2m\tau \right] (U_{A_{i}}^{n-1} \otimes \bar{U}_{A_{i}}^{n-1}) \\ &= \left[n \left(1 - \frac{E}{2} \right) \zeta_{A_{i}}(H) \left(1 - \frac{E}{2} \right) + \frac{n}{2} \frac{E}{2} \zeta_{A_{i}}(H) \frac{E}{2} + \frac{n}{2} \frac{O}{2} \zeta_{A_{i}}(H) \frac{O}{2} \right] (1 - E) + O(1), \end{split}$$
(G11)

where in the last line we have restricted ourselves to the perfect switching cycle, i.e., $n\tau = (\pi/2)$, and neglected any terms in the sum that are not at least O(n).

It is now convenient to rewrite $\zeta_{A_n}(H)$:

$$\zeta_{A_{i}}(H) = \frac{1}{2} \Pi_{A_{i}}[H^{2} \otimes I + I \otimes H^{2} - 2H \otimes H] \Pi_{A_{i}} - \frac{1}{2} [H_{A_{i}}^{2} \otimes P_{A_{i}} + P_{A_{i}} \otimes H_{A_{i}}^{2} - 2H_{A_{i}} \otimes H_{A_{i}}]
= \frac{1}{2} \Pi_{A_{i}}[H^{2} \otimes I + I \otimes H^{2} - 2H \otimes H] \Pi_{A} - E \equiv Z - E,$$
(G12)

where Z has been defined in the last line. We may now combine Eqs. (G11) and (G12) to find

$$\sum_{m=0}^{n-1} (U_A^m \otimes \bar{U}_A^m) \zeta(H) (U_A^{n-1-m} \otimes \bar{U}_A^{n-1-m}) = \left[n \left(1 - \frac{E}{2} \right) (Z - E) \left(1 - \frac{E}{2} \right) + \frac{n}{2} \frac{E}{2} (Z - E) \frac{E}{2} + \frac{n}{2} \frac{O}{2} (Z - E) \frac{O}{2} \right] (1 - E) + O(1)$$

$$= n \left[Z - \frac{EZ}{2} - \frac{ZE}{2} + \frac{3}{8} EZE + \frac{1}{8} OZO - E \right] (1 - E) + O(1)$$

$$= n \left[Z + E - \frac{1}{2} \{ E, Z \} + \frac{1}{8} EZE - \frac{1}{8} OZO \right] + O(1), \tag{G13}$$

where $\{E, Z\} = EZ + ZE$ is the anticommutator.

Now, combining Eqs. (G3) and (G13), we find that the near-Zeno term in Eq. (G3) becomes

$$-n\tau^{2} \sum_{a,b} (P_{a} \otimes P_{a}) \left[Z + E - \frac{1}{2} \{ E, Z \} + \frac{1}{8} E Z E - \frac{1}{8} O Z O \right] (P_{b} \otimes P_{b}). \tag{G14}$$

Considering each of the terms in Eq. (G14), we have

$$\sum_{a,b} (P_a \otimes P_a) Z(P_b \otimes P_b) = \sum_a \deg(a) (P_a \otimes P_a) - \sum_{a,b} P_a H P_b \otimes P_a H P_b, \tag{G15}$$

$$\sum_{a,b} (P_a \otimes P_a) E(P_b \otimes P_b) = \sum_{a \in A_i} P_a \otimes P_a - \sum_{a,b \in A_i} P_a H P_b \otimes P_a H P_b, \tag{G16}$$

$$\begin{split} \sum_{a,b} (P_a \otimes P_a) \bigg[-\frac{1}{2} \{E,Z\} \bigg] (P_b \otimes P_b) &= -\sum_{a \in A_i} [\deg(a) + 1] (P_a \otimes P_a) + \sum_{a,b \in A_i} \bigg(2 + \frac{\deg(a) + \deg(b)}{2} \bigg) P_a H P_b \otimes P_a H P_b \\ &+ \frac{1}{2} \sum_{a \in A^c \mid b \in A_i} (P_a H P_b \otimes P_a H P_b + \text{H.c.}) \end{split}$$

$$+\frac{1}{2}\sum_{a\in A_i^c,b\in A_i}(F_a\Pi F_b\otimes F_a\Pi F_b+\Pi.c.)$$

$$-\frac{1}{2} \sum_{a \in A_i^c, b \in A_i} (P_a H H_{A_i} P_b \otimes P_a H H_{A_i} P_b + \text{H.c.}). \tag{G17}$$

$$\sum_{a,b} (P_a \otimes P_a) \left[\frac{1}{8} EZE \right] (P_b \otimes P_b) = 2 \sum_{a \in A_i} P_a \otimes P_a - 2 \sum_{a,b \in A_i} P_a HP_b \otimes P_a HP_b. \tag{G18}$$

$$\sum_{a,b} (P_a \otimes P_a) \left[-\frac{1}{8} OZO \right] (P_b \otimes P_b) = -2 \sum_{a \in A_i} P_a \otimes P_a + 2 \sum_{a,b \in A_i} P_a H P_b \otimes P_a H P_b. \tag{G19}$$

Finally, we therefore have that \tilde{R}_i becomes

$$\operatorname{case 2:} \left[\tilde{R}_i \right]_{ab} = \begin{cases} \operatorname{deg}(a) & \text{for } a = b \in A_i^c \\ -1 & \text{for } a, b \in A_i^c \text{ and nearest neighbors} \\ -\frac{1}{2} & \text{for } (a \in A_i \text{ and } b \text{ neighbors the adjacent pair in } A_i \text{ that includes } a) \text{ or vice versa} \\ \frac{\operatorname{deg}(a) + \operatorname{deg}(b)}{2} & \text{for } a, b \in A_i \text{ and nearest neighbors} \\ 0 & \text{otherwise.} \end{cases}$$
(G20)

Now, Eqs. (G6) and (G20) may be combined to find the full \tilde{R}_i . Note that on the seam between case 1 and case 2, for example, the element $[\tilde{R}_i]_{ab}$ with a as an orange site in Fig. 16 and b as a blue site, case 1 and case 2 match as required for consistency. Namely, the element $[\tilde{R}_i]_{ab} = -1$ if a, b are nearest neighbors, and 0 otherwise. Furthermore, note that \tilde{R}_i is a zero line-sum matrix. Hence, the rows and columns of $R_{nz,i} = R_i - n\tau^2 \tilde{R}_i$ sum to 1. Furthermore, this implies the rows and columns of R_{nz} also sum to 1 as required for the usage of Eq. (30).

APPENDIX H: DETERMINISTIC HOPPING

Evolution in the Zeno limit with perfect swapping is deterministic. Thus, edge transport and bulk localization can be seen directly.

Figure 17 shows a Lieb lattice with two layers of dynamical unit cells in the y direction and infinitely many in the x direction. The following gives the transport of a particle beginning at any given site after one complete measurement cycle (represented by arrows). Note that after no more than five measurement cycles, each particle returns to either its initial position or its initial position shifted by one dynamical unit cell to the right or left.

(a) Periodic boundary conditions

(i)
$$1 \rightarrow 1$$

(ii)
$$2 \rightarrow 12e^{ik_x} \rightarrow 5 \rightarrow 4 \rightarrow 3 \rightarrow 2$$

(iii)
$$6 \rightarrow 11 \rightarrow 10 \rightarrow 9 \rightarrow 8 \rightarrow 6$$

(iv)
$$7 \rightarrow 7$$

where e^{-ik_x} indicates a shift by one unit cell to the right. Note that after five measurement cycles every particle returns to its initial position in agreement with

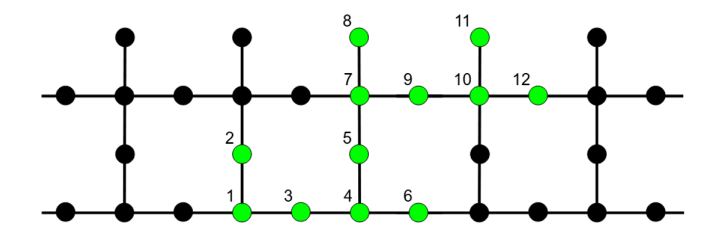


FIG. 17. Lieb lattice with two layers of dynamical unit cells in the *y* direction. The bottom and top of the lattice represent a "flat" and "jagged" edge configuration, respectively.

 $R_{\rm cyc}(k,\theta)^5 = I$, as described below Eq. (28). Now we turn to open boundary conditions.

- (b) Open boundary conditions
 - (i) $1 \rightarrow 6 \rightarrow 1e^{-ik_x}$
 - (ii) $2 \rightarrow 12e^{ik_x} \rightarrow 5 \rightarrow 4 \rightarrow 3 \rightarrow 2$
 - (iii) $7 \rightarrow 7$
 - (iv) $8 \rightarrow 11e^{ik_x} \rightarrow 10e^{ik_x} \rightarrow 9e^{ik_x} \rightarrow 8e^{ik_x}$

Note here that, in contrast to the periodic boundary conditions, there is particle transport in the *x* direction. Namely, particles at sites 1 and 6 shift to the right by one unit cell every two measurement cycles, and particles at 8, 9, 10, and 11 shift to the left one unit cell every four measurement cycles.

- [1] Netanel H. Lindner, Gil Refael, and Victor Galitski, *Floquet Topological Insulator in Semiconductor Quantum wells*, Nat. Phys. **7**, 490 (2011).
- [2] J. W. McIver, B. Schulte, F.-U. Stein, T. Matsuyama, G. Jotzu, G. Meier, and A. Cavalleri, *Light-Induced Anomalous Hall Effect in Graphene*, Nat. Phys. **16**, 38 (2020)
- [3] M. Nuske, L. Broers, B. Schulte, G. Jotzu, S. A. Sato, A. Cavalleri, A. Rubio, J. W. McIver, and L. Mathey, *Floquet Dynamics in Light-Driven Solids*, Phys. Rev. Research 2, 043408 (2020).
- [4] Paraj Titum, Netanel H. Lindner, Mikael C. Rechtsman, and Gil Refael, *Disorder-Induced Floquet Topological Insula*tors, Phys. Rev. Lett. 114, 056801 (2015).
- [5] Arijit Kundu, Mark Rudner, Erez Berg, and Netanel H. Lindner, Quantized Large-Bias Current in the Anomalous Floquet-Anderson Insulator, Phys. Rev. B 101, 041403(R) (2020).
- [6] Frederik Nathan, Dmitry Abanin, Erez Berg, Netanel H. Lindner, and Mark S. Rudner, *Anomalous Floquet Insulators*, Phys. Rev. B 99, 195133 (2019).
- [7] Hoi Chun Po, Lukasz Fidkowski, Takahiro Morimoto, Andrew C. Potter, and Ashvin Vishwanath, *Chiral Floquet Phases of Many-Body Localized Bosons*, Phys. Rev. X 6, 041070 (2016).
- [8] Mark S. Rudner, Netanel H. Lindner, Erez Berg, and Michael Levin, Anomalous Edge States and the Bulk-Edge Correspondence for Periodically Driven Two-Dimensional Systems, Phys. Rev. X 3, 031005 (2013).

- [9] Sthitadhi Roy, J. T. Chalker, I. V. Gornyi, and Yuval Gefen, Measurement-Induced Steering of Quantum Systems, Phys. Rev. Research 2, 033347 (2020).
- [10] Simon Lieu, Max McGinley, and Nigel R. Cooper, *Tenfold Way for Quadratic Lindbladians*, Phys. Rev. Lett. **124**, 040401 (2020).
- [11] T. Müller, S. Diehl, and M. Buchhold, *Measurement-Induced Dark State Phase Transitions in Long-Ranged Fermion Systems*, Phys. Rev. Lett. **128**, 010605 (2022).
- [12] Shengqi Sang and Timothy H. Hsieh, *Measurement-Protected Quantum Phases*, Phys. Rev. Research 3, 023200 (2021).
- [13] Jan Carl Budich, Peter Zoller, and Sebastian Diehl, Dissipative Preparation of Chern Insulators, Phys. Rev. A 91, xxx (2015).
- [14] C.-E. Bardyn, M. A. Baranov, C. V. Kraus, E. Rico, A. İmamoğlu, P. Zoller, and S. Diehl, *Topology by Dissipation*, New J. Phys. 15, 085001 (2013).
- [15] A. Tomadin, S. Diehl, M. D. Lukin, P. Rabl, and P. Zoller, Reservoir Engineering and Dynamical Phase Transitions in Optomechanical Arrays, Phys. Rev. A 86, 033821 (2012).
- [16] Piotr Sierant, Giuliano Chiriacò, Federica M. Surace, Shraddha Sharma, Xhek Turkeshi, Marcello Dalmonte, Rosario Fazio, and Guido Pagano, Dissipative Floquet Dynamics: from Steady State to Measurement Induced Criticality in Trapped-Ion Chains, Quantum 6, 638 (2022).
- [17] Longwen Zhou and Jiangbin Gong, Non-Hermitian Floquet Topological Phases with Arbitrarily Many Real-Quasienergy Edge States, Phys. Rev. B **98**, 205417 (2018).
- [18] Yaodong Li and Matthew P. A. Fisher, Statistical Mechanics of Quantum Error Correcting Codes, Phys. Rev. B 103, 104306 (2021).
- [19] M. Buchhold, Y. Minoguchi, A. Altland, and S. Diehl, Effective Theory for the Measurement-Induced Phase Transition of Dirac Fermions, Phys. Rev. X 11, 041004 (2021).
- [20] Yimu Bao, Soonwon Choi, and Ehud Altman, *Theory of the Phase Transition in Random Unitary Circuits with Measurements*, Phys. Rev. B **101**, 104301 (2020).
- [21] Amos Chan, Rahul M. Nandkishore, Michael Pretko, and Graeme Smith, *Unitary-Projective Entanglement Dynamics*, Phys. Rev. B **99**, 224307 (2019).
- [22] Michael J. Gullans and David A. Huse, *Dynamical Purification Phase Transition Induced by Quantum Measurements*, Phys. Rev. X **10**, 041020 (2020).
- [23] Chao-Ming Jian, Yi-Zhuang You, Romain Vasseur, and Andreas W. W. Ludwig, *Measurement-Induced Criticality* in Random Quantum Circuits, Phys. Rev. B 101, 104302 (2020).
- [24] M. Szyniszewski, A. Romito, and H. Schomerus, Entanglement Transition from Variable-Strength Weak Measurements, Phys. Rev. B 100, 064204 (2019).
- [25] A. Zabalo, M. J. Gullans, J. H. Wilson, R. Vasseur, A. W. W. Ludwig, S. Gopalakrishnan, David A. Huse, and J. H. Pixley, *Operator Scaling Dimensions and Multifractality at Measurement-Induced Transitions*, Phys. Rev. Lett. 128, 050602 (2022).
- [26] Brian Skinner, Jonathan Ruhman, and Adam Nahum, Measurement-Induced Phase Transitions in the Dynamics of Entanglement, Phys. Rev. X 9, 031009 (2019).

- [27] Yaodong Li, Xiao Chen, and Matthew P.A. Fisher, Quantum Zeno Effect and the Many-Body Entanglement Transition, Phys. Rev. B 98, 205136 (2018).
- [28] Yaodong Li, Xiao Chen, and Matthew P. A. Fisher, Measurement-Driven Entanglement Transition in Hybrid Quantum Circuits, Phys. Rev. B 100, 134306 (2019).
- [29] Michael J. Gullans and David A. Huse, Scalable Probes of Measurement-Induced Criticality, Phys. Rev. Lett. 125, 070606 (2020).
- [30] Soonwon Choi, Yimu Bao, Xiao-Liang Qi, and Ehud Altman, *Quantum Error Correction in Scrambling Dynamics and Measurement-Induced Phase Transition*, Phys. Rev. Lett. **125**, 030505 (2020).
- [31] Romain Vasseur, Andrew C. Potter, Yi-Zhuang You, and Andreas W. W. Ludwig, Entanglement Transitions from Holographic Random Tensor Networks, Phys. Rev. B 100, 134203 (2019).
- [32] Chao-Ming Jian, Yi-Zhuang You, Romain Vasseur, and Andreas W. W. Ludwig, *Measurement-Induced Criticality* in Random Quantum Circuits, Phys. Rev. B 101, 104302 (2020).
- [33] Shengqi Sang and Timothy H. Hsieh, *Measurement-Protected Quantum Phases*, Phys. Rev. Research 3, 023200 (2021).
- [34] Davide Rossini and Ettore Vicari, Measurement-Induced Dynamics of Many-Body Systems at Quantum Criticality, Phys. Rev. B 102, 035119 (2020).
- [35] Aidan Zabalo, Michael J. Gullans, Justin H. Wilson, Sarang Gopalakrishnan, David A. Huse, and J. H. Pixley, *Critical Properties of the Measurement-Induced Transition in Random Quantum Circuits*, Phys. Rev. B **101**, 060301(R) (2020).
- [36] Ruihua Fan, Sagar Vijay, Ashvin Vishwanath, and Yi-Zhuang You, Self-Organized Error Correction in Random Unitary Circuits with Measurement, Phys. Rev. B 103, 174309 (2021).
- [37] Matteo Ippoliti, Michael J. Gullans, Sarang Gopalakrishnan, David A. Huse, and Vedika Khemani, *Entanglement Phase Transitions in Measurement-Only Dynamics*, Phys. Rev. X 11, 011030 (2021).
- [38] Ali Lavasani, Yahya Alavirad, and Maissam Barkeshli, Measurement-Induced Topological Entanglement Transitions in Symmetric Random Quantum Circuits, Nat. Phys. 17, 342 (2021).
- [39] Shengqi Sang, Yaodong Li, Tianci Zhou, Xiao Chen, Timothy H. Hsieh, and Matthew P. A. Fisher, *Entanglement Negativity at Measurement-Induced Criticality*, PRX Quantum **2**, 030313 (2021).
- [40] Bowen Shi, Xin Dai, and Yuan-Ming Lu, Entanglement Negativity at the Critical Point of Measurement-Driven Transition, arXiv:2012.00040.
- [41] Valentin Gebhart, Kyrylo Snizhko, Thomas Wellens, Andreas Buchleitner, Alessandro Romito, and Yuval Gefen, Topological Transition in Measurement-Induced Geometric Phases, Proc. Natl. Acad. Sci. U.S.A. 117, 5706 (2020).
- [42] Oliver Lunt and Arijeet Pal, Measurement-Induced Entanglement Transitions in Many-Body Localized Systems, Phys. Rev. Research 2, 043072 (2020).

- [43] Amos Chan, Rahul M. Nandkishore, Michael Pretko, and Graeme Smith, *Unitary-Projective Entanglement Dynamics*, Phys. Rev. B **99**, 224307 (2019).
- [44] Xiangyu Cao, Antoine Tilloy, and Andrea De Luca, Entanglement in a Fermion Chain under Continuous Monitoring, SciPost Phys. 7, 24 (2019).
- [45] O. Alberton, M. Buchhold, and S. Diehl, *Entanglement Transition in a Monitored Free-Fermion Chain: From Extended Criticality to Area Law*, Phys. Rev. Lett. **126**, 170602 (2021).
- [46] Israel Klich, Closed Hierarchies and Non-Equilibrium Steady States of Driven Systems, Ann. Phys. (Amsterdam) 2019) 66, 404).
- [47] Matthew Wampler, Peter Schauss, Eugene B. Kolomeisky, and Israel Klich, *Quantum Wakes in Lattice Fermions*, Phys. Rev. Research **3**, 033112 (2021).
- [48] K. v. Klitzing, G. Dorda, and M. Pepper, New Method for High-Accuracy Determination of the Fine-Structure Constant Based on Quantized Hall Resistance, Phys. Rev. Lett. 45, 494 (1980).
- [49] Jainendra K. Jain, *Composite Fermions* (Cambridge University Press, Cambridge, England, 2007).
- [50] The analogy is incomplete, however, in the Zeno limit of rapid measurements where the measurement-induced chirality is a completely classical effect (as opposed to the quantum Hall effect where coherence plays a key role). The effect, however, does persist in the regime of less frequent measurements where the consequences of quantum coherence become important.
- [51] P. Facchi and S. Pascazio, Quantum Zeno Dynamics: Mathematical and Physical Aspects, J. Phys. A 41, 493001 (2008).
- [52] Onur Hosten, Matthew T. Rakher, Julio T. Barreiro, Nicholas A. Peters, and Paul G. Kwiat, *Counterfactual Quantum Computation through Quantum Interrogation*, Nature (London) **439**, 949 (2006).
- [53] Yuan Cao, Yu-Huai Li, Zhu Cao, Juan Yin, Yu-Ao Chen, Hua-Lei Yin, Teng-Yun Chen, Xiongfeng Ma, Cheng-Zhi Peng, and Jian-Wei Pan, *Direct Counterfactual Communi*cation via Quantum Zeno Effect, Proc. Natl. Acad. Sci. U.S.A. 114, 4920 (2017).
- [54] Bo Yan, Steven A. Moses, Bryce Gadway, Jacob P. Covey, Kaden R. A. Hazzard, Ana Maria Rey, Deborah S. Jin, and Jun Ye, Observation of Dipolar Spin-Exchange Interactions with Lattice-Confined Polar Molecules, Nature (London) 501, 521 (2013).
- [55] B. Zhu, B. Gadway, M. Foss-Feig, J. Schachenmayer, M. L. Wall, K. R. A. Hazzard, B. Yan, S. A. Moses, J. P. Covey, D. S. Jin, J. Ye, M. Holland, and A. M. Rey, Suppressing the Loss of Ultracold Molecules via the Continuous Quantum Zeno Effect, Phys. Rev. Lett. 112, 070404 (2014).
- [56] Wayne M. Itano, D. J. Heinzen, J. J. Bollinger, and D. J. Wineland, *Quantum Zeno Effect*, Phys. Rev. A 41, 2295 (1990).
- [57] M. C. Fischer, B. Gutiérrez-Medina, and M. G. Raizen, Observation of the Quantum Zeno and Anti-Zeno Effects in an Unstable System, Phys. Rev. Lett. 87, 040402 (2001).

- [58] Erik W. Streed, Jongchul Mun, Micah Boyd, Gretchen K. Campbell, Patrick Medley, Wolfgang Ketterle, and David E. Pritchard, Continuous and Pulsed Quantum Zeno Effect, Phys. Rev. Lett. 97, 260402 (2006).
- [59] Svetlana V. Kilina, Amanda J. Neukirch, Bradley F. Habenicht, Dmitri S. Kilin, and Oleg V. Prezhdo, Quantum Zeno Effect Rationalizes the Phonon Bottleneck in Semiconductor Quantum Dots, Phys. Rev. Lett. 110, 180404 (2013).
- [60] F. Schäfer, I. Herrera, S. Cherukattil, C. Lovecchio, F. S. Cataliotti, F. Caruso, and A. Smerzi, *Experimental Realization of Quantum Zeno Dynamics*, Nat. Commun. **5**, 3194 (2014).
- [61] Adrien Signoles, Adrien Facon, Dorian Grosso, Igor Dotsenko, Serge Haroche, Jean-Michel Raimond, Michel Brune, and Sébastien Gleyzes, Confined Quantum Zeno Dynamics of a Watched Atomic Arrow, Nat. Phys. 10, 715 (2014).
- [62] P. M. Harrington, J. T. Monroe, and K. W. Murch, Quantum Zeno Effects from Measurement Controlled Qubit-Bath Interactions, Phys. Rev. Lett. 118, 240401 (2017).
- [63] Paraj Titum, Erez Berg, Mark S. Rudner, Gil Refael, and Netanel H. Lindner, *Anomalous Floquet-Anderson Insula*tor as a Nonadiabatic Quantized Charge Pump, Phys. Rev. X 6, 021013 (2016).

- [64] Yoichi Ando, Topological Insulator Materials, J. Phys. Soc. Jpn. 82, 102001 (2013).
- [65] Mark S. Rudner, Netanel H. Lindner, Erez Berg, and Michael Levin, Anomalous Edge States and the Bulk-Edge Correspondence for Periodically Driven Two-Dimensional Systems, Phys. Rev. X 3, 031005 (2013).
- [66] Cherie R. Kagan, Efrat Lifshitz, Edward H. Sargent, and Dmitri V. Talapin, *Building Devices from Colloidal Quantum Dots*, Science 353, 6302 (2016).
- [67] Maxwell F. Parsons, Florian Huber, Anton Mazurenko, Christie S. Chiu, Widagdo Setiawan, Katherine Wooley-Brown, Sebastian Blatt, and Markus Greiner, Site-Resolved Imaging of Fermionic ⁶Li in an Optical Lattice, Phys. Rev. Lett. 114, 213002 (2015).
- [68] Peter T. Brown, Debayan Mitra, Elmer Guardado-Sanchez, Reza Nourafkan, Alexis Reymbaut, Charles-David Hébert, Simon Bergeron, A.-M. S. Tremblay, Jure Kokalj, David A. Huse, Peter Schauß, and Waseem S. Bakr, *Bad Metallic Transport in a Cold Atom Fermi-Hubbard System*, Science 363, 379 (2019).
- [69] Jayadev Vijayan, Pimonpan Sompet, Guillaume Salomon, Joannis Koepsell, Sarah Hirthe, Annabelle Bohrdt, Fabian Grusdt, Immanuel Bloch, and Christian Gross, *Time-Resolved Observation of Spin-Charge Deconfinement in Fermionic Hubbard Chains*, Science 367, 186 (2020).